The Astrophysical Journal, 759:29 (16pp), 2012 November 1 doi:10.1088/0004-637X/759/1/29

A *HST*/WFC3-IR MORPHOLOGICAL SURVEY OF GALAXIES AT $z = 1.5$–3.6. II. THE RELATION BETWEEN MORPHOLOGY AND GAS-PHASE KINEMATICS*

David R. Law[1,6], Charles C. Steidel[2], Alice E. Shapley[3], Sarah R. Nagy[3], Naveen A. Reddy[4], and Dawn K. Erb[5]
[1] Dunlap Institute for Astronomy and Astrophysics, University of Toronto, 50 St. George Street, Toronto, Ontario M5S 3H4, Canada; drlaw@di.utoronto.ca
[2] Department of Astronomy, California Institute of Technology, MS 249-17, Pasadena, CA 91125, USA; ccs@astro.caltech.edu
[3] Department of Physics and Astronomy, University of California, Los Angeles, CA 90095, USA; aes@astro.ucla.edu, snagy@ucla.edu
[4] Department of Physics and Astronomy, University of California, Riverside, CA 92521, USA
[5] Department of Physics, University of Wisconsin–Milwaukee, P.O. Box 413, Milwaukee, WI 53201, USA
Received 2012 June 28; accepted 2012 September 11; published 2012 October 15

ABSTRACT

We analyze rest-frame optical morphologies and gas-phase kinematics as traced by rest-frame far-UV and optical spectra for a sample of 204 star-forming galaxies in the redshift range $z \sim 2$–3 drawn from the Keck Baryonic Structure Survey. We find that spectroscopic properties and gas-phase kinematics are closely linked to morphology: compact galaxies with semimajor axis radii $r \lesssim 2$ kpc are substantially more likely than their larger counterparts to exhibit Lyα in emission. Although Lyα emission strength varies widely within galaxies of a given morphological type, all but one of 19 galaxies with Lyα equivalent width $W_{\mathrm{Ly}\alpha} > 20$ Å have compact and/or multiple-component morphologies with $r \leqslant 2.5$ kpc. The velocity structure of absorption lines in the galactic continuum spectra also varies as a function of morphology. Galaxies of all morphological types drive similarly strong outflows (as traced by the blue wing of interstellar absorption line features), but the outflows of larger galaxies are less highly ionized and exhibit larger optical depth at the systemic redshift that may correspond to a decreasing efficiency of feedback in evacuating gas from the galaxy. This $v \sim 0$ km s^{-1} gas is responsible both for shifting the mean absorption line redshift and attenuating $W_{\mathrm{Ly}\alpha}$ (via a longer resonant scattering path) in galaxies with larger rest-optical half-light radii. In contrast to galaxies at lower redshifts, there is no evidence for a correlation between outflow velocity and inclination, suggesting that outflows from these puffy and irregular systems may be poorly collimated. Our observations are broadly consistent with theoretical models of inside-out growth of galaxies in the young universe, in which typical $z \sim 2$–3 star-forming galaxies are predominantly unstable, dispersion-dominated, systems fueled by rapid gas accretion that later form extended rotationally supported disks when stabilized by a sufficiently massive stellar component.

Key words: galaxies: fundamental parameters – galaxies: high-redshift – galaxies: structure

Online-only material: color figures

1. INTRODUCTION

Galaxy evolution is a process driven largely by the lifecycle of gas and its accretion, conversion into stars, and eventual loss via supernova-driven winds. During the peak epoch of galaxy formation ($z \sim 2$–3; Dickinson et al. 2003; Reddy et al. 2008; Zhu et al. 2009) those systems that dominate the luminosity function are especially gas-rich, with gas frequently accounting for 50% or more of the total baryonic mass (e.g., Erb et al. 2006c; Tacconi et al. 2010). This large supply of hydrogen fuels sustained star formation rates (SFRs) commonly $\sim 30\,M_\odot$ yr^{-1} (e.g., Erb et al. 2006b; Wuyts et al. 2011) and SFR surface densities peaking above $\sim 1\,M_\odot$ yr^{-1} kpc^{-2} (e.g., Genzel et al. 2011) that are comparable to those in transient starbursts in the modern universe (Kennicutt 1998b).

The mechanisms by which these galaxies acquire such large quantities of gas are uncertain; although gas has traditionally been assumed to accrete primarily through mergers (e.g., Robertson et al. 2006) and "hot mode" accretion via virial shocks (e.g., Rees & Ostriker 1977; White & Rees 1978; White & Frenk 1991), some recent arguments suggest that semi-continuous cold accretion from cosmological filaments (e.g., Kereš et al. 2005, 2009; Dekel et al. 2009; Bournaud & Elmegreen 2009; Ceverino et al. 2010) may be required to sustain the observed SFR and produce the structures observed at $z \sim 2$. As discussed by Reddy et al. (2012) however, star formation at $z \sim 2$–3 appears to have been an inefficient process, indicating that SFR is unlikely to have been limited primarily by the cold gas accretion rate.

In contrast to galaxies in the nearby universe, $z \sim 2$ star-forming galaxies do not exhibit regular spiral structure (with some notable exceptions; Law et al. 2012a) and instead tend to be compact, triaxial systems consisting of one or more irregularly shaped clumps of emission (e.g., Conselice et al. 2005; Elmegreen et al. 2005; Ravindranath et al. 2006; Law et al. 2012b, and references therein). In many of the most massive galaxies ($M_* \gtrsim 3 \times 10^{10}\,M_\odot$) such clumps may be embedded in low surface brightness structures reminiscent of thick disks with typical scale heights $h_z \sim 1$ kpc (e.g., Elmegreen & Elmegreen 2006; Genzel et al. 2006, 2008; Förster Schreiber et al. 2011a, 2011b) sustained by their large vertical velocity dispersions (e.g., Genzel et al. 2006; Law et al. 2007b, 2009; Förster Schreiber et al. 2009; Swinbank et al. 2011).

The large cold gas fractions of these galaxies appear to play a significant role in their dynamical and morphological evolution. Simulations (e.g., Noguchi 1999; Immeli et al. 2004a, 2004b; Bournaud et al. 2007; Bournaud & Elmegreen 2009) indicate that such gas-rich galaxies should be highly unstable to fragmentation, forming clumps similar to those observed

* Based in part on data obtained at the W. M. Keck Observatory, which is operated as a scientific partnership among the California Institute of Technology, the University of California, and NASA, and was made possible by the generous financial support of the W. M. Keck Foundation.
[6] Dunlap Fellow.

which may either migrate to form a central bulge (Immeli et al. 2004a, 2004b; Elmegreen et al. 2008; Ceverino et al. 2010) or be rapidly disrupted by stellar feedback (Wuyts et al. 2012). A reliable understanding of the relation between galactic stellar morphology and its gas-phase properties is therefore critical for constraining models of galaxy formation in the young universe.

While observational signatures of *infalling* gas (whether hot or cold mode) have proven subtle and difficult to detect (e.g., van de Voort & Schaye 2012; although cf. Rauch et al. 2011 and Kulas et al. 2012), the intense star formation of the galaxies gives rise to ubiquitous and well-studied galactic-scale *outflows* evident in rest-frame UV spectra (e.g., Shapley et al. 2003; Weiner et al. 2009; Steidel et al. 2010). These outflows are frequently powerful enough to drive enriched gas to the virial radius and beyond with mass loss rates comparable to or exceeding the SFR (Pettini et al. 2000; Erb 2008; Steidel et al. 2010). Numerous authors (e.g., Shapley et al. 2003; Pentericci et al. 2010; Kornei et al. 2010; Steidel et al. 2010; Jones et al. 2012) have therefore sought to use the information about optical depth, covering fraction, geometry, and gas kinematics encoded within such spectra to learn about the mechanisms by which cold gas is coupled to feedback and physical observables such as stellar mass, SFR, and stellar population age. Efforts to understand the role of the gas in shaping the evolution of galaxy morphology however (e.g., Law et al. 2007a; Pentericci et al. 2010) have historically been limited in their ability to test current galaxy formation models by the lack of availability of high-resolution rest-frame optical imaging tracing the bulk of the stellar mass.

In the present contribution, we combine rest-frame optical imaging of a large sample of $z \sim 2$ star-forming galaxies recently obtained with the WFC3 camera on board the *Hubble Space Telescope* (*HST*) with ground-based rest-UV spectroscopy to investigate the relation between galaxy morphology and gas-phase kinematics. In Section 2 we describe the target galaxy sample and detail the methods by which morphological, photometric, and spectroscopic data were obtained. We discuss the Lyα emission properties of the sample in Section 3, and the structure of major interstellar absorption lines arising in outflowing cold gas in Section 4, highlighting the changing velocity substructure of the absorption lines as a function of galaxy morphology. We discuss the implications of our findings for the evolution of typical $z \sim 2$–3 star-forming galaxies in Section 5, combining our results with recent observations from integral-field unit (IFU) kinematic surveys. We summarize our conclusions in Section 6.

Throughout our analysis, we adopt a standard ΛCDM cosmology based on the seven-year *WMAP* results (Komatsu et al. 2011) in which $H_0 = 70.4$ km s^{-1} Mpc^{-1}, $\Omega_M = 0.272$, and $\Omega_\Lambda = 0.728$.

2. OBSERVATIONAL DATA

Our galaxy sample is drawn from the Keck Baryonic Structure Survey (KBSS; Trainor & Steidel 2012), a catalog of $z \sim 1.5$–3.6 star-forming galaxies selected according to optical $U_nG\mathcal{R}$ color (Steidel et al. 2003, 2004; Adelberger et al. 2004) and confirmed using rest-UV spectroscopy. These galaxies typically lie near sightlines to hyperluminous background QSOs ($z_{\rm QSO} \sim 2.7$) scattered widely across the sky. We define two specific samples of galaxies used in our analysis.

Parent sample. A sample of 204 galaxies with *HST*/WFC3 imaging data, magnitudes $H_{160} \lesssim 24$ AB, and redshifts $z \sim 1.5$–3.5 (see Figure 1) derived from rest-UV spectroscopy.

HAHQ subsample. A subgroup of 35 galaxies from the parent sample for which the rest-UV spectroscopy is particularly high quality ("uvqual" $\geqslant 1$; see Section 2.2) and secure systemic redshifts in the range $z = 2.0$–2.5 (see Figure 1) have been obtained from Hα nebular emission line spectroscopy.

2.1. Rest-optical Morphologies

As part of *HST* Cycle 17 program GO-11694, we obtained WFC3/IR imaging of 306 $U_nG\mathcal{R}$ color-selected star-forming galaxies with spectroscopic redshifts in the range $z = 1.5$–3.6 drawn from the KBSS. The details of these observations have been described at length by Law et al. (2012a; hereafter "Paper I"). In brief, we used the F160W ($\lambda_{\rm eff} = 15369$ Å) filter to trace rest-frame optical emission ($\lambda \sim 3400$–6100 Å for the parent sample, $\lambda \sim 4400$–5100 Å for the Hα high-quality (HAHQ) sample). Our data reach a depth of 27.9 AB for a 5σ detection within a 0.2 arcsec radius aperture (representing a total of 8100 s integration in each pointing), and have a point-spread function (PSF) FWHM of 0.″18 that corresponds to 1.5 kpc at $z \sim 2$.

The morphologies consist of three qualitative types. As defined in Paper I, these are as follows.

Type 1. Single nucleated component with little to no low surface brightness emission.

Type 2. Two or more distinct nucleated components of comparable magnitude and little to no low surface brightness emission.

Type 3. Extended objects with non-axisymmetric low surface brightness features.

Numerous morphological statistics have been defined in the literature that attempt to encapsulate this range of morphologies quantitatively. In Paper I, we calculated seven of the most widely used such statistics for each of the galaxies in our WFC3 imaging fields. These statistics are as follows.

r. Semimajor axis radius derived from fitting Sérsic (1963) models convolved with the observational PSF to the F160W light profile using the GALFIT (Peng et al. 2002, 2010) analysis package. We also define the circularized effective radius ($r_{\rm e} = r\sqrt{b/a}$) for consistency with previous analyses, where b/a is the apparent minor/major axis ratio.

n. Radial index of the best-fit Sérsic model profile.

G. Gini statistic (Abraham et al. 2003; Lotz et al. 2004) quantifying the cumulative flux distribution among the galaxy pixels.

M_{20}. Second-order moment of the spatial distribution of the light profile (Lotz et al. 2004, 2006).

C. Concentration index of the flux distribution about the center of the galaxy (Bershady et al. 2000; Conselice 2003).

A. Asymmetry index (Schade et al. 1995; Conselice et al. 2000) quantifying the 180° rotational asymmetry of the galaxy.

Ψ. Multiplicity index (Law et al. 2007a) quantifying the "work" required to assemble the distribution of pixel fluxes within a galaxy (distinguishing single-component from irregular and multiple-component sources).

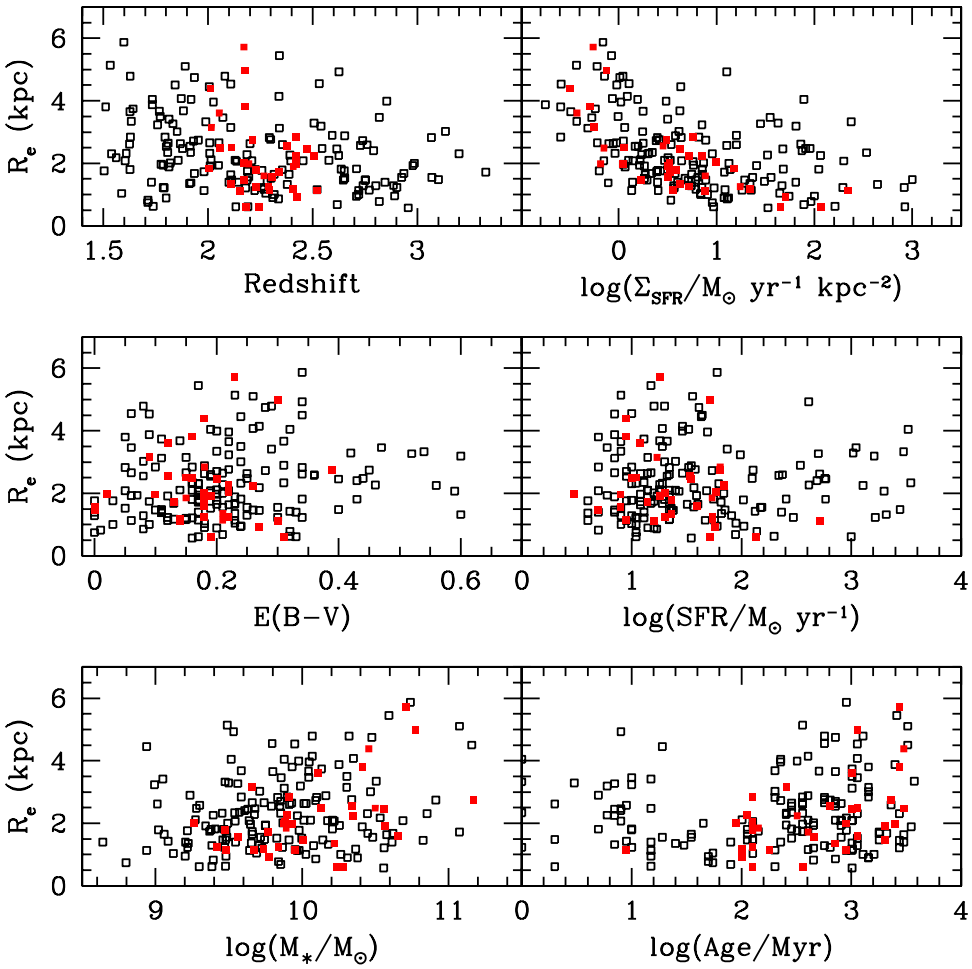

Figure 1. Redshifts, stellar population parameters, and effective radii derived for the parent (black open boxes) and Hα high-quality (HAHQ; red filled boxes) samples of 204 and 35 galaxies, respectively. The two samples have significant overlap, but the HAHQ sample is the product of a complicated selection function resulting in a more restricted redshift range and marginally larger stellar masses and population ages than the parent population on average.

(A color version of this figure is available in the online journal.)

Although the first two morphological statistics (r, n) assume a parametric model convolved with the observational PSF, the latter five (G, M_{20}, C, A, Ψ) are non-parameterically derived from the spatial arrangement of individual pixel fluxes. The values calculated for these five statistics depend systematically on the adopted segmentation map defining which pixels are considered to be part of a given galaxy. Our approach is placed on the systematic reference frame of Lotz et al. (2008a, 2008b, and references therein) using the transformations described in Appendix A.1 of Paper I.

All seven morphological statistics are robust for galaxies with $H_{160} \lesssim 24$ AB, and show systematic bias at fainter magnitudes (see Appendix A.2 of Paper I). We therefore restrict our attention in the present contribution to those 204 galaxies with $H_{160} \leqslant 24.0$ and no evidence of a QSO or active galactic nucleus (AGN) in their UV spectra (Section 2.2) or broadband photometry (Section 2.4). As derived in Paper I, typical uncertainties for individual galaxies are $\sim$2% in r, 15% in n, 3% in G, 4% in M_{20}, 11% in C, 22% in A, and 21% in Ψ.

2.2. Rest-UV Spectroscopy

Rest-frame UV spectra for each of our galaxies have been obtained using the LRIS multi-slit spectrograph on Keck I. Details concerning the observational setup, data reduction, and calibration process of these spectra have been presented at length elsewhere in the literature (e.g., Shapley et al. 2003; Steidel et al. 2010, and references therein). In general, individual spectra represent integration times $\sim$1.5 hr with characteristic velocity resolution $\sigma_{\rm res} \approx 160$ km s^{-1}. These spectra vary considerably in quality according to both the intrinsic brightness of the target galaxy and the conditions under which particular slit masks were observed. We sort the galaxies according to the quality of their spectra, assigning them quality indices "uvqual" ranging from 0 (one or two spectroscopic features identified with relatively low confidence) to 3 (multiple strong spectroscopic features identified with extremely high confidence).

The limited signal-to-noise ratio (S/N) of even the highest-quality spectra, however, means that it is typically only possible to estimate the mean interstellar absorption (emission) line redshift $z_{\rm IS}$ ($z_{\rm EM}$) for individual galaxies. In order to investigate the detailed structure of spectral lines, it is necessary to stack together multiple spectra to reach higher S/Ns. This stacking process is described in detail by Steidel et al. (2010), and includes Doppler-correcting each spectrum to the rest frame,[7] resampling to a common 0.33 Å pixel^{-1} spectral dispersion,

[7] Where available we use the nebular emission line redshift derived from rest-optical spectroscopy as detailed in Section 2.3, otherwise we adopt the prescriptions given by Steidel et al. (2010).

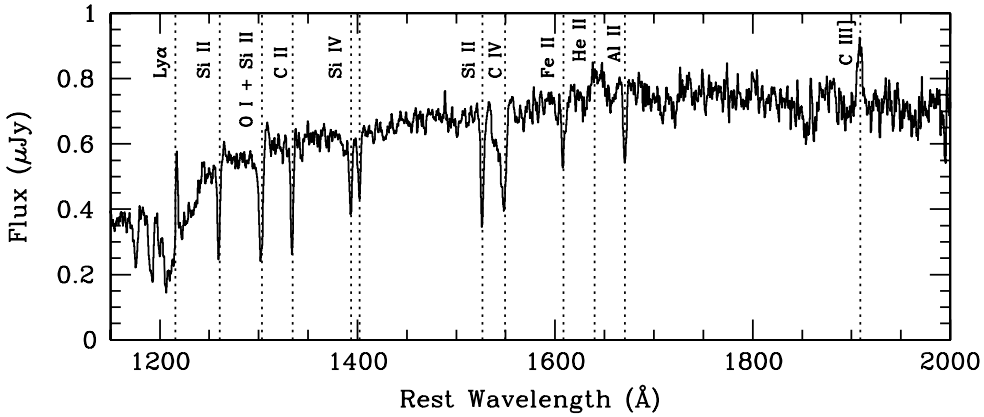

Figure 2. Flux-calibrated rest-UV Keck/LRIS-B spectrum constructed from stacking 204 star-forming galaxies in our parent sample in the redshift range $1.5 < z < 3.5$. Vertical dotted lines indicate the fiducial wavelengths of major emission and/or absorption line transitions.

and rescaling to a common mode in the wavelength range $\lambda \sim 1250$–1500 Å before combining individual spectra using a sigma-clipped mean algorithm.

In Figure 2, we show the composite spectrum for the 204 galaxies in our parent sample. This composite spectrum exhibits a mixture of Lyα absorption and emission, deep blended interstellar absorption features due to various metal species in the galactic interstellar medium (ISM), and a host of weaker features due to stellar photospheric absorption and fine structure emission. These absorption features are typically blueshifted with respect to the systemic redshift (corresponding to absorption arising in the near side of an outflowing galactic wind), while Lyα emission is redshifted (corresponding to off-resonance backscattering from the far side of the outflow). As described at length by Steidel et al. (2010; see also Kulas et al. 2012), this outflow is likely composed of discrete gas clouds whose expansion velocities increase with galactocentric radius.

2.3. Rest-optical Spectroscopy

Although the rest-UV spectra give an indication of the redshift of the interstellar absorption lines $z_{\rm IS}$, it is not possible to perform a detailed analysis of the kinematic structure of the outflowing gas without knowing the systemic redshift $z_{\rm sys}$ of the galaxy as well. We therefore define the HAHQ subsample of galaxies with particularly robust measurements of $z_{\rm IS}$ and for which accurate (uncertainty $\sim$60 km s^{-1}; Steidel et al. 2010) systemic redshifts have been derived from Hα nebular emission using a combination of long-slit Keck/NIRSPEC (Erb et al. 2006b), integral-field Keck/OSIRIS (Law et al. 2007b, 2009; Wright et al. 2009), and Very Large Telescope/SINFONI (Förster Schreiber et al. 2009) spectroscopy. The HAHQ sample represents the subset of 35 of the 89 galaxies considered by Steidel et al. (2010) for which *HST*/WFC3 morphologies have been obtained.

2.4. Stellar Population Models

Extensive KBSS ancillary data exist for our target galaxies, typically including deep ground-based optical and infrared J/K_s photometry, and in some cases *Spitzer* IRAC and/or MIPS photometry. In combination with H_{160} magnitudes derived from the *HST*/WFC3 imaging data, the long-wavelength photometry permits us to construct stellar population models by fitting the broadband spectral energy distribution (SED) of each galaxy as detailed in Paper I (see also Shapley et al. 2001, 2005; Erb et al. 2006c; Reddy et al. 2006, 2010). In brief, we fit S. Charlot & G. Bruzual (2012, in preparation) stellar population synthesis models in combination with a Chabrier (2003) initial mass function, Calzetti et al. (2000) extinction law, and a constant ($\tau = \infty$) star formation history using a customized IDL code (Reddy et al. 2012). Monte Carlo tests for the 204-galaxy parent sample indicate that the mean fractional uncertainties in derived values for $E(B-V)$, age, SFR, and M_* are $\langle \sigma_x/x \rangle = 0.3$, 0.6, 0.5, and 0.4, respectively (consistent with previous measurements for the larger KBSS sample by Shapley et al. 2005, Erb et al. 2006b, and Reddy et al. 2012).

As illustrated in Figure 1, galaxies in the parent sample have stellar masses in the range $M_* \sim 10^9$–$10^{11}\,M_\odot$, SFRs $\sim 30\,M_\odot$ yr^{-1}, and moderate color excess $E(B-V) \sim 0.0$–0.4. The HAHQ subsample is biased relative to the parent sample by the requirement of both detecting Hα emission and observing a high-quality UV spectrum (favoring UV-bright objects), and therefore has a slightly larger mean stellar mass ($\langle \log M_*/M_\odot \rangle_{\rm HAHQ} = 10.1 \pm 0.4$ versus $\langle \log M_*/M_\odot \rangle_{\rm Parent} = 9.9 \pm 0.5$).[8]

3. Lyα EMISSION

Lyα emission originates deep within individual star-forming regions and is resonantly scattered throughout the ISM until either being absorbed on a dust grain or redshifted sufficiently far off-resonance that it can escape the galaxy. Although almost all star-forming galaxies appear to have Lyα-emitting halos on large angular scales (Steidel et al. 2011), the Lyα profile of the central few kpc traced by slit spectra is dependent upon the structure, kinematics, and ionization properties of each galaxy and its interstellar and circumgalactic medium. Substantial efforts have been made over the last decade to attempt to disentangle these various effects and connect the central Lyα line profile with global stellar population properties both for narrowband-selected Lyα emitters (LAEs; e.g., Gawiser et al. 2007) and for star-forming galaxies selected via broadband optical color. Shapley et al. (2003), for instance, found that $z \sim 3$ Lyman break galaxies (LBGs) with stronger Lyα emission tend to have lower SFR, bluer UV continua, and weaker low-ionization interstellar absorption lines. Similar results were found for $z \sim 2$ star-forming galaxies by Erb et al. (2006a) and Law et al. (2007a), who noted that galaxies with stellar masses $M_* > 10^{10}\,M_\odot$ on average have weaker Lyα emission than do galaxies with $M_* < 10^{10}\,M_\odot$, and at $z \sim 4$ by Jones et al. (2012). These

[8] 1σ values represent standard deviation about the mean.

results were borne out by the more detailed analysis of Steidel et al. (2010), which demonstrated that Lyα emission is both weaker and more strongly redshifted from the systemic velocity in galaxies with high baryonic mass, consistent with the picture that Lyα emission from the deepest gravitational potential wells must scatter further from resonance before being able to escape. Using a similarly selected sample of LBGs at $z = 2.5$–3.5, Pentericci et al. (2010) found comparable results, showing that galaxies without Lyα emission tend to be more massive and dustier, although these authors observed that stellar population ages and SFRs did not depend strongly on Lyα emission characteristics.

The relation between Lyα emission and rest-frame UV galaxy morphology has previously been investigated by Law et al. (2007a) and Pentericci et al. (2010) (see also Bond et al. 2009; Malhotra et al. 2012). Law et al. (2007a) found that Lyα emission was correlated with the Gini coefficient in the sense that high-G (i.e., strongly nucleated) systems were more likely to exhibit Lyα emission, which we previously ascribed to the lower quantity of dust in strongly nucleated galaxies. Although Pentericci et al. (2010) found no significant correlation of Lyα emission with any of the non-parametric morphological indices (C, G, A, or M_{20}), these authors noted that while galaxies with weak or no Lyα emission spanned a range of projected angular sizes, galaxies with strong Lyα emission tended to be exclusively small.

In Section 3.1, we discuss the probability that galaxies within our sample exhibit Lyα emission as a function of various physical properties, and expand our discussion in Section 3.2 to consider the trends in emission line strength within the Lyα-emitting subset.

3.1. Probability of Lyα Emission

We divide the parent sample into two groups according to whether Lyα emission is present (71 galaxies) or not (117 galaxies) in the UV spectrum of each galaxy.[9] The first of these two groups includes galaxies with Lyα emission of any strength, including those with a small emission peak superimposed on a large Lyα absorption trough. We later discuss the properties of a "Lyα-bright" subgroup which meets the $W_{\rm Ly\alpha} > 20$ Å selection criterion used by dedicated surveys of LAEs (e.g., Gawiser et al. 2007).

In Table 1 we list probabilities calculated using the nonparametric Kolmogorov–Smirnov (K-S) test to evaluate whether the two groups are statistically consistent with the null hypotheses that they are drawn from the same distribution of stellar mass, SFR, morphology, etc. We find that SFR and the morphological parameters M_{20}, C, A, Ψ, and n are poor predictors of the likelihood of observing Lyα emission from a galaxy; galaxies with and without Lyα in emission have statistically indistinguishable distributions. In contrast, the null hypothesis is rejected at greater than 94%–95% confidence when we examine the mass, age, color excess, G, or r distributions for galaxies both with and without Lyα in emission. These correlations are in the sense that galaxies with Lyα emission on average are smaller, may have slightly lower mass ($\langle \log(M_*/M_\odot) \rangle = 9.82$ versus 9.96), and slightly younger ages (500 versus 800 Myr), and are less dusty ($\langle E(B-V) \rangle = 0.18$ versus 0.23) than galaxies with no Lyα emission. These results are broadly consistent with relations that have already been established by Shapley et al. (2003), Erb et al. (2006a), Law et al. (2007a), Steidel et al. (2010), and Pentericci et al. (2010).

Table 1
K-S Probability That Galaxies with and without Lyα Emission are Drawn from Different Distributions[a]

Quantity	$P_{\rm KS}$
M_*[b]	**6%**
Age[c]	**8%**
SFR[d]	99%
$\Sigma_{\rm SFR}$[e]	**1%**
$E(B-V)$[f]	**3%**
G	**8%**
M_{20}	83%
C	26%
A	99%
Ψ	56%
r[g]	**3%**
$r_{\rm e}$[h]	**0.5%**
n	15%
b/a[i]	59%
H_{160}	12%

Notes.
[a] All values are one minus the probability at which the null hypothesis (that the quantities are drawn from a statistically identical distribution of the indicated parameter) is ruled out. The sample size is 188 galaxies. Bold values are statistically significant.
[b] Stellar mass, estimated from SED fitting.
[c] Average population age from a constant SFR SED model.
[d] Star formation rate measured from SED fitting.
[e] Average star formation rate surface density $\Sigma_{\rm SFR} = {\rm SFR}/\pi r_{\rm e}^2$.
[f] Color excess due to dust extinction from a constant SFR SED model.
[g] GALFIT semimajor axis radius.
[h] GALFIT circularized effective radius.
[i] Morphological minor/major axis ratio.

We note, however, that Kornei et al. (2010) studied the Lyα properties of $z \sim 3$ LBGs and found a conflicting result that those with $W_{\rm Ly\alpha} > 20$ Å tended to have stellar populations slightly *older* than their non-emitting kin, which was hypothesized to indicate that LAEs may represent a later stage in galaxy evolution in which supernova-driven outflows have reduced the dust covering fraction (see also Shapley et al. 2001).[10] The difference with our present findings may partly reflect the different mean redshift range of the samples or may indicate that the relation between Lyα emission strength and stellar population age is simply too weak (96% rejection of the null hypothesis) to measure consistently given typical uncertainties in the derived ages of individual galaxies. Indeed, while Pentericci et al. (2010) concurred that LAEs tended to be slightly younger than similarly selected non-emitters on average, these authors too noted that the correlation was only marginally significant.

As indicated by Table 1, within our sample of star-forming galaxies there is no statistically significant correlation between

[9] We rejected 16 galaxies in the redshift range $z = 1.5$–1.7 from our sample since Lyα emission at these redshifts does not fall within the LRIS UV spectral range.

[10] Kornei et al. (2010) used an equivalent width measure $W_{\rm Ly\alpha} > 20$ Å to define their Lyα-emitting population, in contrast to our simple criterion that there be any measurable Lyα emission. However, our results are qualitatively unchanged if we instead consider the Lyα-bright subset of galaxies with $W_{\rm Ly\alpha} > 20$ Å.

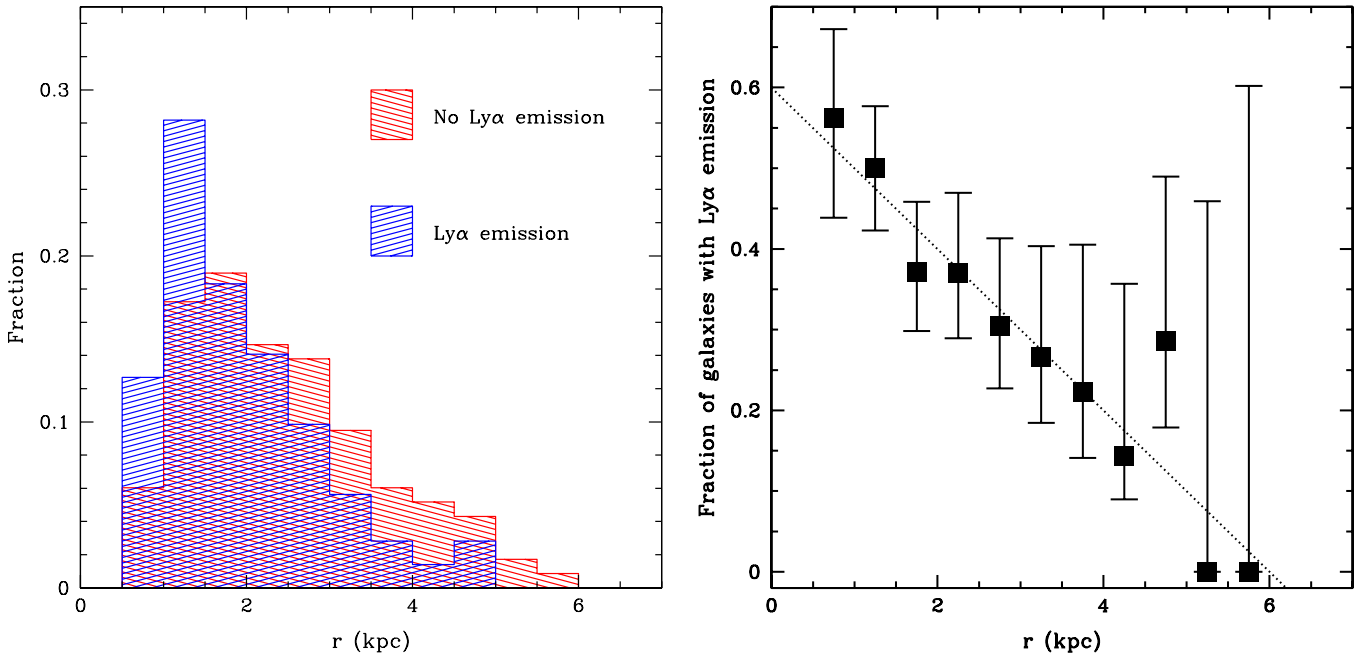

Figure 3. Left panel: histogram of semimajor axis radius r for galaxies with and without Lyα emission component in the 183 galaxies of the parent sample for which the LRIS spectral range includes the Lyα transition. Fractions shown are relative to the total number of galaxies with (71 galaxies) and without (117 galaxies) Lyα emission, respectively. Right panel: fraction of galaxies in each radial bin that show Lyα emission; 1σ uncertainties are estimated using a binomial probability distribution. The dashed line indicates a least-squares fit of the form $y = 0.60$–$0.10 \times x$ to the data; a zero slope is disfavored with $\sim 3\sigma$ confidence.

(A color version of this figure is available in the online journal.)

the presence/absence of Lyα emission and the morphological indices C, A, M_{20}, Ψ, or n. Similar to the result obtained by Law et al. (2007a), there is a relation (92% confidence) between Lyα emission and the Gini parameter G in the sense that galaxies with Lyα emission tend to have marginally more strongly nucleated light profiles in the rest-frame optical. This trend does not appear to be of statistical significance, however, as the mean values of G for galaxies with and without Lyα emission respectively differ by only $\sim 1\sigma$ ($\langle G \rangle_{\mathrm{Ly}\alpha} = 0.49 \pm 0.01$ versus $\langle G \rangle_{\mathrm{NoLy}\alpha} = 0.478 \pm 0.005$).[11]

In contrast, the presence of Lyα emission is strongly correlated with the morphological semimajor axis radius r, circularized radius r_e, and (by construction) the SFR surface density $\Sigma_{\mathrm{SFR}} = \mathrm{SFR}/\pi r_e^2$. These correlations are significant at the 97%–99% confidence level, comparable to or stronger than the well-known anti-correlation between Lyα emission and dust content $E(B-V)$. Similarly to the rest-UV angular size relation noted by Pentericci et al. (2010), galaxies with Lyα in emission are more likely than non-emitters to have $r < 2.5$ kpc (74% versus 56%), and the galaxies with $r < 2.5$ kpc in our sample are twice as likely (41% versus 24%) as those with $r > 2.5$ kpc to have Lyα in emission (see Figure 3). This is unlikely to be due to any intrinsic correlation between semimajor axis radius and dust content; although r and $E(B-V)$ of the parent sample are marginally correlated at the $\sim 2\sigma$ level (based on the Spearman rank correlation test), this correlation is in the sense that larger galaxies tend to be marginally *less* dusty.

We illustrate the spectroscopic difference between large- and small-r galaxies by stacking the halves of the parent and HAHQ samples with the smallest and largest semimajor axis radii (Figure 4).[12] The Lyα emission equivalent width $W_{\mathrm{Ly}\alpha}$ of

[11] Here the uncertainties represent the $1/\sqrt{N}$ uncertainty in the mean of each sample.

[12] The median radius used to divide the samples is 2.08 kpc and 1.98 kpc for the parent and HAHQ samples, respectively.

Table 2
Correlation of $W_{\mathrm{Ly}\alpha}$ and Galaxy Properties[a]

Quantity	Standard Deviation
M_*[b]	−1.7
Age[c]	0.5
SFR[d]	**−2.4**
Σ_{SFR}[e]	−0.2
$E(B-V)$[f]	**−2.4**
G	−0.2
M_{20}	**2.2**
C	−0.7
A	1.4
Ψ	1.6
r[g]	**−2.1**
r_e[h]	**−2.3**
n	−1.1
b/a[i]	−1.9
H_{160}	1.4

Notes. [a] All values are the number of standard deviations from the null hypothesis that the quantities are uncorrelated, based on a Spearman rank correlation test. Positive (negative) values indicate positive (negative) correlation between the quantities (i.e., larger r corresponds to lower $W_{\mathrm{Ly}\alpha}$). The sample size is 71 galaxies. Bold values are statistically significant.
[b] Stellar mass, estimated from SED fitting.
[c] Average population age from a constant SFR SED model.
[d] Star formation rate measured from SED fitting.
[e] Average star formation rate surface density $\Sigma_{\mathrm{SFR}} = \mathrm{SFR}/\pi r_e^2$.
[f] Color excess due to dust extinction from a constant SFR SED model.
[g] GALFIT semimajor axis radius.
[h] GALFIT circularized effective radius.
[i] Morphological minor/major axis ratio.

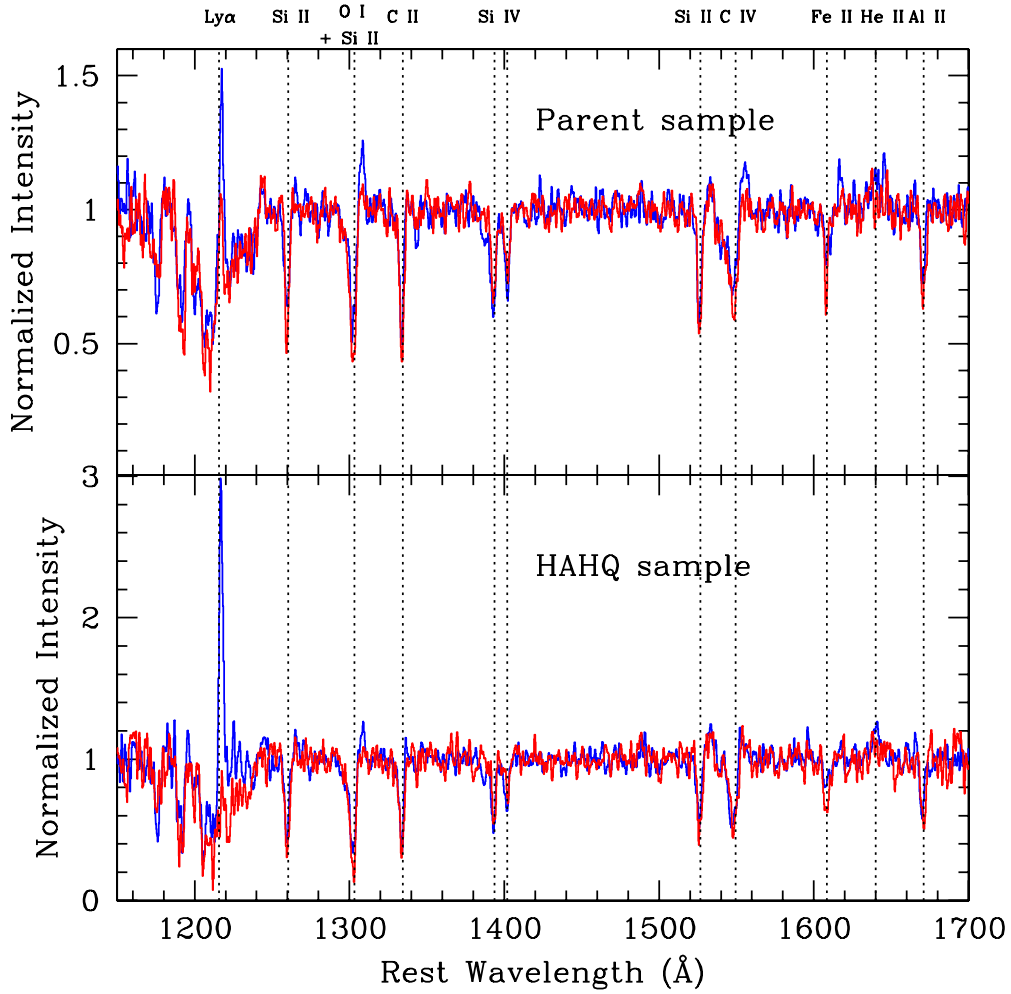

Figure 4. Continuum-normalized stacked Keck/LRIS-B UV spectra of the 50% of galaxies with smallest (blue lines) and largest (red lines) sizes for the parent (200 galaxies) and HAHQ (35 galaxies) galaxy samples (note differing vertical scales). The vertical dotted lines indicate the wavelengths of major spectral features arising from a combination of low/high-ionization interstellar absorption and various emission mechanisms. While not labeled, the emission feature at ∼1300 Å is the fine structure emission line Si II∗λ1309. Note the drastic difference in Lyα profiles and varying depths of the low-ionization absorption features.

(A color version of this figure is available in the online journal.)

the large- and small-r stacks is 1.3 Å and 2.6 Å respectively in the parent sample, representing a factor ∼2 increase in the mean Lyα emission strength.[13] This difference is even more pronounced in the HAHQ subsample, increasing by a factor ∼10 from the large-r ($W_{\rm Ly\alpha} = 0.7$ Å) to small-r ($W_{\rm Ly\alpha} = 6.7$ Å) stacks, corresponding to a K-S probability of ∼0.2% that the radii of galaxies with and without Lyα in emission are drawn from the same distribution.

3.2. Strength of Lyα Emission

Within the group of galaxies with Lyα in emission similar correlations exist between Lyα emission *strength* and physical galaxy properties. We compute the emission line equivalent width $W_{\rm Ly\alpha}$ relative to the continuum level in our flux-calibrated spectra for each of the 71 galaxies with such emission in the parent sample.[14] In Table 2, we tabulate the correlations between $W_{\rm Ly\alpha}$ and physical galaxy properties in terms of the number of standard deviations from the null hypothesis (that the two variables are uncorrelated) using the Spearman rank correlation test. The factors most strongly influencing $W_{\rm Ly\alpha}$ are the dust content $E(B-V)$ of a galaxy (2.4σ), its total SFR (2.4σ),[15] and its physical size (2.3σ), in the sense that larger, dustier galaxies with higher SFR have lower $W_{\rm Ly\alpha}$.

We illustrate these three trends in Figure 5. Similarly to previous studies (e.g., Shapley et al. 2003; Kornei et al. 2010; Pentericci et al. 2010), we find that galaxies with the strongest $W_{\rm Ly\alpha}$ tend to contain lower than average quantities of dust and have lower SFRs. Additionally, galaxies with large rest-optical sizes ($r \gtrsim 3$ kpc) tend to have $W_{\rm Ly\alpha} < 20$ Å, while the smallest galaxies ($r \lesssim 2$ kpc) exhibit a much wider range in equivalent width from $W_{\rm Ly\alpha} = 0$–180 Å. Of the 19 star-forming galaxies in our optical-color-selected sample with $W_{\rm Ly\alpha} \gtrsim 20$ Å all but one have rest-optical radii $r \leqslant 2.5$ kpc and Type I and II morphologies (i.e., one or two nucleated components to the light profile with little to no extended and/or diffuse low surface brightness emission in the WFC3 imaging data; see

[13] By comparison, Monte Carlo tests stacking randomly selected halves of the galaxy sample indicate that the $W_{\rm Ly\alpha}$ of the stacks typically vary by ∼30% for the parent sample, and by a factor ∼2 for the HAHQ subsample.

[14] Based on an analysis of ∼1000 galaxies with Lyα emission in the KBSS, we estimate that uncertainties on $W_{\rm Ly\alpha}$ for individual galaxies are typically ∼4 Å.

[15] Although the SFR has no statistically significant relation to the probability of observing Lyα in emission, for the subsample of galaxies with Lyα in emission we find the SFR to be correlated with the strength $W_{\rm Ly\alpha}$ of the emission.

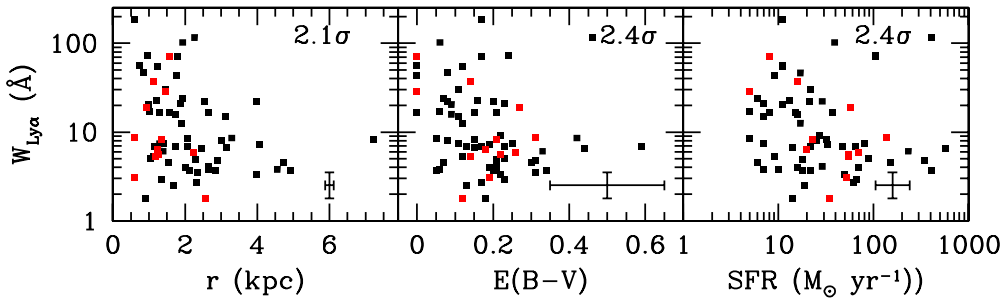

Figure 5. Lyα emission equivalent width $W_{\rm Ly\alpha}$ as a function of rest-optical semimajor axis radius r, dust content $E(B-V)$, and SED-derived star formation rate for the 71 galaxies with measurable Lyα emission in the parent sample (black points). Red points denote the 12 Lyα-emitting galaxies that are also in the HAHQ subsample. $W_{\rm Ly\alpha}$ decreases with r, $E(B-V)$, and SFR; the significance of the correlations as estimated from the Spearman rank correlation test is indicated in each panel. Error bars in the lower right corner of each panel indicate the characteristic uncertainty of individual points.

(A color version of this figure is available in the online journal.)

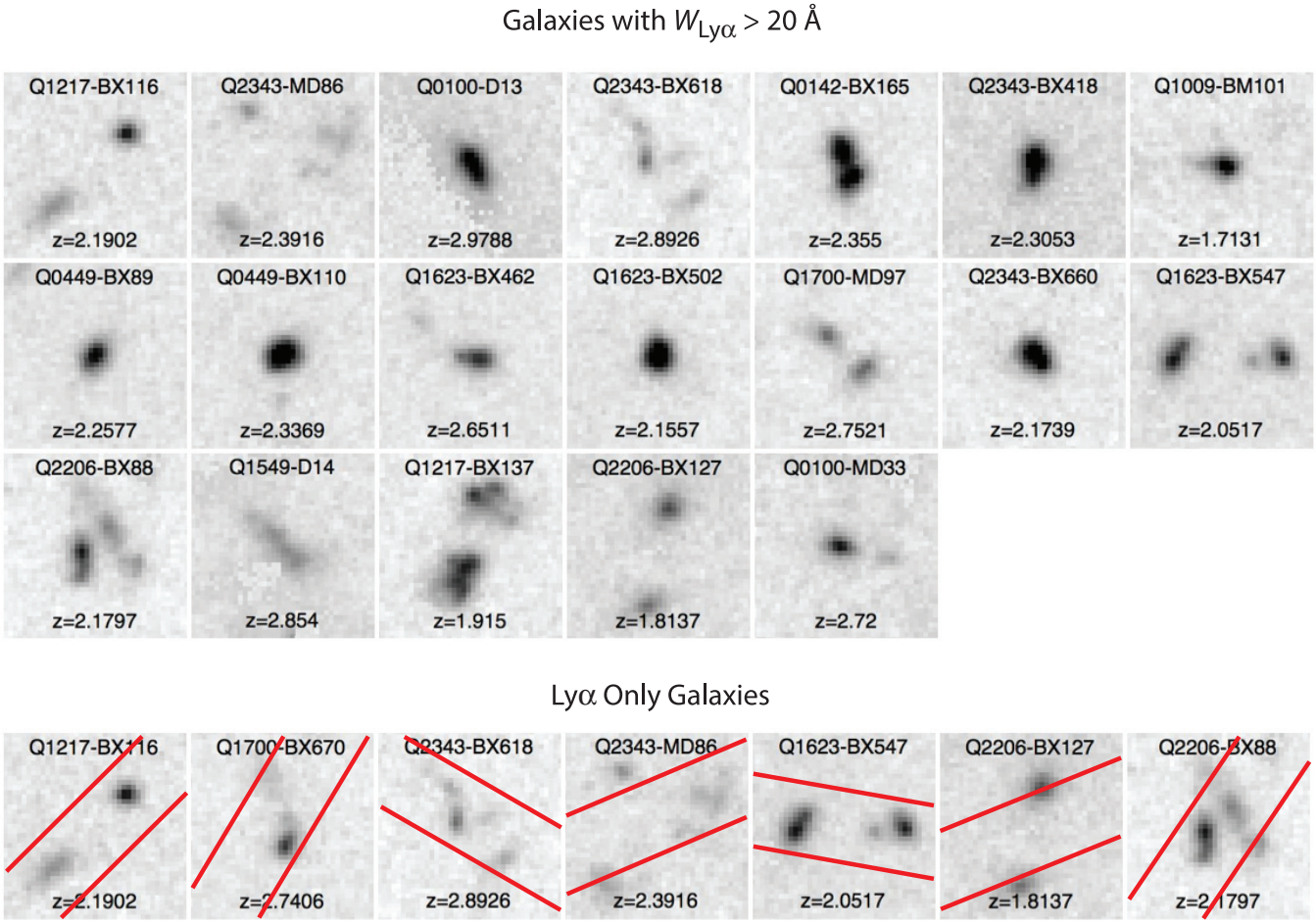

Figure 6. *HST*/WFC3 F160W rest-optical morphologies of the 19 galaxies in the parent sample with Lyα emission equivalent width $W_{\rm Ly\alpha} > 20$ Å (top panel), and of the 7 galaxies in the parent sample with Lyα emission but no absorption features in their rest-UV spectra. Both sets of galaxies are sorted in order of decreasing $W_{\rm Ly\alpha}$. Note that 18 of the 19 galaxies in the top panel are compact with Type I or II morphology, while all galaxies in the lower panel have Type II morphology. Images are 3″ to a side, and oriented with north up and east to the left and centered on the F160W flux centroid. The color map has been inverted and uses an arcsinh stretch with the black point set to 27.3 AB pixel^{-1} (21.8 AB arcsec^{-2}). Red lines in the lower panel indicate the width and position angle of the LRIS-B slit during observations of each galaxy.

(A color version of this figure is available in the online journal.)

Figure 6). The correlation between Lyα equivalent width and optical semimajor axis radius is independent of the correlation with $E(B-V)$; r and $E(B-V)$ are consistent with the null hypothesis of being uncorrelated (0.1σ rejection of the null hypothesis using the Spearman rank correlation test), and confining our sample to a narrow range of values in $E(B-V)$ results in a similarly strong trend of $W_{\rm Ly\alpha}$ with r after accounting for the reduced sample size.

Combining our results with those previously published in the literature, the broad picture of $z \sim 2$–3 LAEs is therefore relatively clear. Compared to star-forming galaxies at this epoch with negligible Lyα emission, galaxies with a measurable Lyα emission component tend to be physically smaller systems with lower stellar mass and less dust, lower SFRs, and a slightly greater degree of nucleation in the rest-frame UV and optical light distribution.

3.3. Galaxies with Exclusively Lyα Emission

Most commonly, galaxies with visible Lyα emission also show some absorption features in their rest-UV spectra as well (albeit frequently weak; see discussion by Shapley et al. 2003). Of the 71 galaxies in the parent sample with Lyα emission, 7 do not have any identifiable absorption features (even in a composite stack). While the Lyα emission equivalent widths for these sources range over a factor ∼10 ($W_{Ly\alpha}$ = 17–184 Å), all seven have Type II morphologies composed of two or more widely separated clumps (see Figure 6), accounting for nearly half of the 17 total galaxies in the parent sample with Lyα emission and Type II morphology. By comparison, 100% of the 28 (26) galaxies with Type I (III) morphology and Lyα emission have visible absorption features in their UV spectra, indicating that multi-component morphology is a strong factor in determining whether absorption line features will be observed in rest-UV spectra.[16]

Morphological indices measuring the two-dimensional distribution of the light from a galaxy (e.g., A, M_{20}, Ψ) therefore easily identify galaxies with exclusively Lyα emission in their rest-UV spectra and suggest that these multi-component galaxies are prime major-merger candidates. If these galaxies are indeed mergers caught in the nearby-pair phase, the disturbed ISM of the combined system may result in a reduced gas covering fraction, making it easier for resonantly scattered Lyα emission to escape from the system. However, Type II galaxies are not intrinsically brighter in Lyα emission than Type I or III galaxies; instead, the only significant difference is that Type II galaxies are less likely to have absorption lines in their UV spectra. A simpler explanation may be that when galaxies with multiple components separated by distances ∼1 arcsec are observed with ground-based spectrographs the slit tends to be placed midway between the two components, thereby systematically reducing the S/N of the continuum emission against which absorption features are measured. As illustrated in Figure 6, in ∼50% of cases the majority of the rest-UV continuum flux is expected to fall outside the slit based on the position angles used for the LRIS spectroscopy; even in cases for which the slit was aligned approximately along the separation vector (e.g., Q1623-BX547) the greater effective area over which the light is distributed may still increase the noise in the continuum such that the observations are systematically biased against the detection of absorption lines.

4. METAL LINE FEATURES

The deepest absorption lines in the rest-UV spectra are the Si II, O I, C II, Fe II, and Al II lines that arise in the metal-enriched neutral ISM, which typically trace massive galactic-scale outflows driven by the intensely starbursting galaxy. As noted in many previous publications (e.g., Shapley et al. 2003) there is generally an anti-correlation between Lyα emission and interstellar absorption line strength; since the metal transitions are optically thick, declining absorption line strength indicates a declining gas velocity dispersion and/or covering fraction, which also permits a greater Lyα escape fraction.

In order to understand the physical mechanisms underlying variations in absorption line strength in greater detail we focus on the HAHQ sample for which accurate systemic redshifts have been obtained from rest-optical nebular emission. The 35 galaxies in our HAHQ sample represent the subset of the 73 galaxies previously considered by Steidel et al. (2010) for which *HST*/WFC3 rest-optical imaging data have now been obtained. In their larger sample, Steidel et al. (2010) demonstrated that there is a correlation between baryonic galaxy mass M_{bary} and Δv_{IS}, the mean velocity offset of the interstellar absorption lines (z_{IS}) from the systemic redshift ($z_{H\alpha}$):

$$\Delta v_{IS} = c(z_{IS} - z_{sys})/(1 + z_{sys}). \quad (1)$$

Using the Spearman rank correlation test, Steidel et al. (2010) found that the null hypothesis (that Δv_{IS} and M_{bary} are uncorrelated) could be ruled out at 2.7σ significance. We repeat the calculations of Steidel et al. (2010) using an estimate of $M_{bary} = M_* + M_{gas}$, where M_* is the stellar mass derived in Paper I and M_{gas} is the gas mass estimated using NIRSPEC and/or OSIRIS Hα fluxes in combination with the Kennicutt–Schmidt law (Kennicutt 1998a; see discussion by Erb et al. 2006c). In Table 3, we list the confidence at which the null hypothesis for zero correlation can be rejected for Δv_{IS}

Table 3
Correlations of Bulk Outflow Velocity and Galaxy Properties[a]

Quantity	Standard Deviation
M_{gas}[b]	0.6
M_*[c]	1.6
M_{bar}[d]	1.5
Age[e]	1.9
SFR[f]	−0.9
Σ_{SFR}[g]	−2.1
$E(B-V)$[h]	0.7
G	−1.7
M_{20}	1.6
C	−1.3
A	1.0
Ψ	1.7
r[i]	2.6
r_e[j]	2.3
n	−1.6
b/a[k]	−0.3
H_{160}	0.3

Notes.
[a] All values are the number of standard deviations from the null hypothesis that the quantities are uncorrelated, based on a Spearman rank correlation test. Positive (negative) values indicate positive (negative) correlation between the quantities (i.e., larger r corresponds to weaker outflows (less negative Δv_{IS}). The sample size is 35 galaxies.
[b] Cold gas mass, estimated from the star formation surface density and the observed Hα size, as in Erb et al. (2006c).
[c] Stellar mass, estimated from SED fitting.
[d] Total baryonic mass $M_{bar} = M_* + M_{gas}$.
[e] Average population age from a constant SFR SED model.
[f] Star formation rate measured from SED fitting.
[g] Average star formation rate surface density $\Sigma_{SFR} = SFR/\pi r_e^2$.
[h] Color excess due to dust extinction from a constant SFR SED model.
[i] GALFIT semimajor axis radius.
[j] GALFIT circularized effective radius.
[k] Morphological minor/major axis ratio.

[16] The fraction of galaxies with Type II morphology and no Lyα emission that do not have visible rest-UV absorption features is not possible to determine, since by definition such galaxies would not have spectroscopically confirmed redshifts.

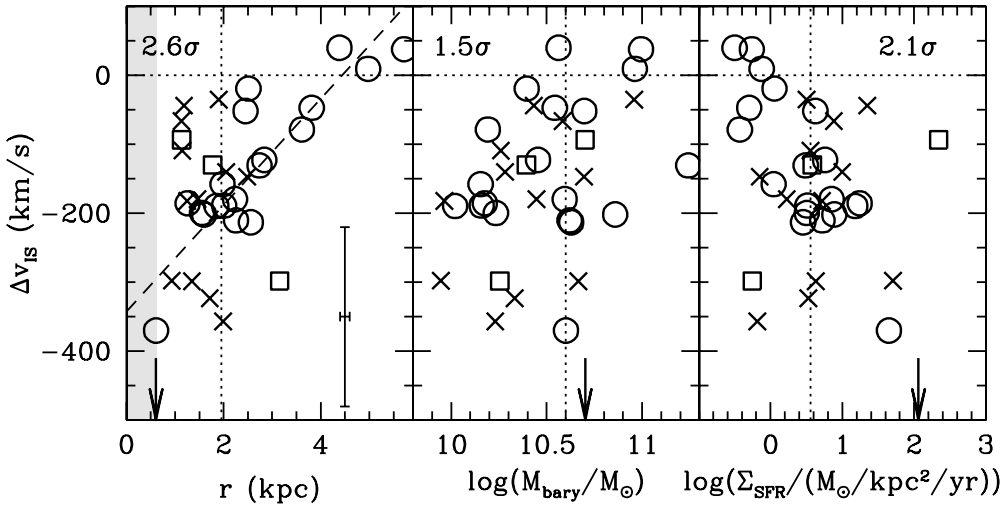

Figure 7. Mean rest-frame velocity offset $\Delta v_{\rm IS}$ between the systemic (Hα) redshift $z_{\rm H\alpha}$ and the low-ionization interstellar absorption line redshift $z_{\rm IS}$ as a function of major-axis galaxy size r (left panel), baryonic mass (middle panel), and SFR surface density $\Sigma_{\rm SFR}$ (right panel) for the subset of 35 galaxies with systemic redshifts from Hα observations and high-quality UV spectra. The arrow indicates the location of Q2343-BX453 ($\Delta v_{\rm IS} = -944\,{\rm km\,s^{-1}}$) which along with Q2343-BX587 lies in the region for which r is unresolved at the 3σ level (gray shaded region). Crosses, open boxes, and open circles represent galaxies with morphological Types I, II, and III, respectively. The vertical dotted lines in the left (right) hand panel divide the sample into two equal-size bins of large-radius and small-radius (large $\Sigma_{\rm SFR}$ and small $\Sigma_{\rm SFR}$) galaxies; the vertical dotted line in the middle panel represents a similar division made according to baryonic mass by Steidel et al. (2010). Negative/positive values of $\Delta v_{\rm IS}$ formally correspond to outflows/inflows, respectively; note how galaxies with the strongest mean outflow velocities tend to be the smallest with the largest $\Sigma_{\rm SFR}$ while the three largest galaxies all have positive $\Delta v_{\rm IS}$. The dashed line indicates a linear least-squares fit to the data: $\Delta v_{\rm IS} = (77(r/{\rm kpc}) - 342)\,{\rm km\,s^{-1}}$.

versus a variety of morphological and other physical properties. As expected we recover the sense of the previous correlation noted by Steidel et al. (2010) between $\Delta v_{\rm IS}$ and total baryonic mass (Figure 7, middle panel), although this correlation has a significance of only 1.5σ; random resampling tests indicate that this lower significance is consistent with the lower total number of galaxies in our sample than in Steidel et al. (2010).

4.1. Correlation of Low-ionization Absorption Line Strength with Semimajor Axis Radius

We find that $\Delta v_{\rm IS}$ correlates with the semimajor axis radius r with a statistical significance of 2.6σ in the sense that the largest velocity differences (i.e., most negative $\Delta v_{\rm IS}$) are observed for the smallest (Type I) galaxies, while the largest (Type III) galaxies have mean gas-phase velocities consistent with 0 km s^{-1} (Figure 7, left panel). Combining measurements from the individual low-ionization absorption lines (except Fe II λ1608, which is significantly weaker and noisier than the other transitions) we find that $\langle \Delta v_{\rm IS} \rangle = -226 \pm 49$ km s^{-1} for the small-radius half of the HAHQ sample ($r < 1.95$ kpc) compared to $\langle \Delta v_{\rm IS} \rangle = -125 \pm 25\,{\rm km\,s^{-1}}$ for the large-radius half ($r > 1.95$ kpc).[17] We illustrate this trend visually in Figure 8; when sorted according to $\Delta v_{\rm IS}$, galaxies with the smallest (blue boxes) and largest (red boxes) sizes are clearly distinguished.

Adopting uncertainties of $\sim$130 km s^{-1} in $\Delta v_{\rm IS}$ and $\sim$0.1 kpc in r for each galaxy (Steidel et al. 2010; Paper I), we use a least-squares routine to fit a first-order polynomial to the data and obtain the average relation

$$\Delta v_{\rm IS} = \left(77\frac{r}{\rm kpc} - 342\right)\,{\rm km\,s^{-1}}. \quad (2)$$

We stress, however, that $\Delta v_{\rm IS}$ does not characterize the outflow velocity of a particular galaxy, but rather represents the centroid of a single-component fit to interstellar absorption lines that are a complex blend of multiple components. In Figure 9 we show the stacked, continuum-normalized spectra for the small- and large-radius subsamples (solid blue/red lines respectively) in zoomed-in regions around the major low-ionization gas absorption lines. Careful inspection of Figure 9 suggests that the low-ionization absorption lines in both low-r and high-r stacks have similar optical depths in their blue wings, indicating that both have outflowing gas tracing a similar range of velocities. Rather, the major difference is the growth of an absorption component centered at $v \approx 0$ km s^{-1} in the large-radius sample that shifts the centroid of the absorption line profile closer to the systemic velocity (see particularly Al II λ1671) and increases the depth of composite absorption line profiles even when precise systemic redshifts are unknown (e.g., Figure 4, top panel). This finding is similar to that described by Steidel et al. (2010; see also Weiner et al. 2009) who found that galaxies below a threshold $M_{\rm bary} \approx 4 \times 10^{10}\,M_\odot$ lack the $v \sim 0$ km s^{-1} component to the low-ionization interstellar absorption lines present in higher-mass galaxies.

Following the formalism adopted by Steidel et al. (2010), we define the additional optical depth $\Delta\tau(v)$ that would need to be added to the low-r composite galaxy spectrum in order to produce an absorption line profile identical to the high-r composite spectrum:

$$I_{\rm hr}(v) = I_{\rm lr}(v)e^{-\Delta\tau(v)}, \quad (3)$$

where $I_{\rm hr}(v)$ and $I_{\rm lr}(v)$ are the spectral intensity of the high-r and low-r halves of the HAHQ sample, respectively. In Figure 10, we show $\Delta\tau(v)$ for the three strongest unblended low-ionization absorption lines (Si II λ1260, C II λ1334, and Si II λ1526) along with the average composite for all three lines combined. Although there is some variation between the individual lines, the composite exhibits a significant broad absorption component from $\sim$−400 to $\sim$+400 km s^{-1} in galaxies with the largest semimajor axis radii. As discussed at length by Steidel et al. (2010), this component could represent either infalling

[17] Uncertainties represent 1σ uncertainties in the mean combining $\Delta v_{\rm IS}$ of individual galaxy spectra.

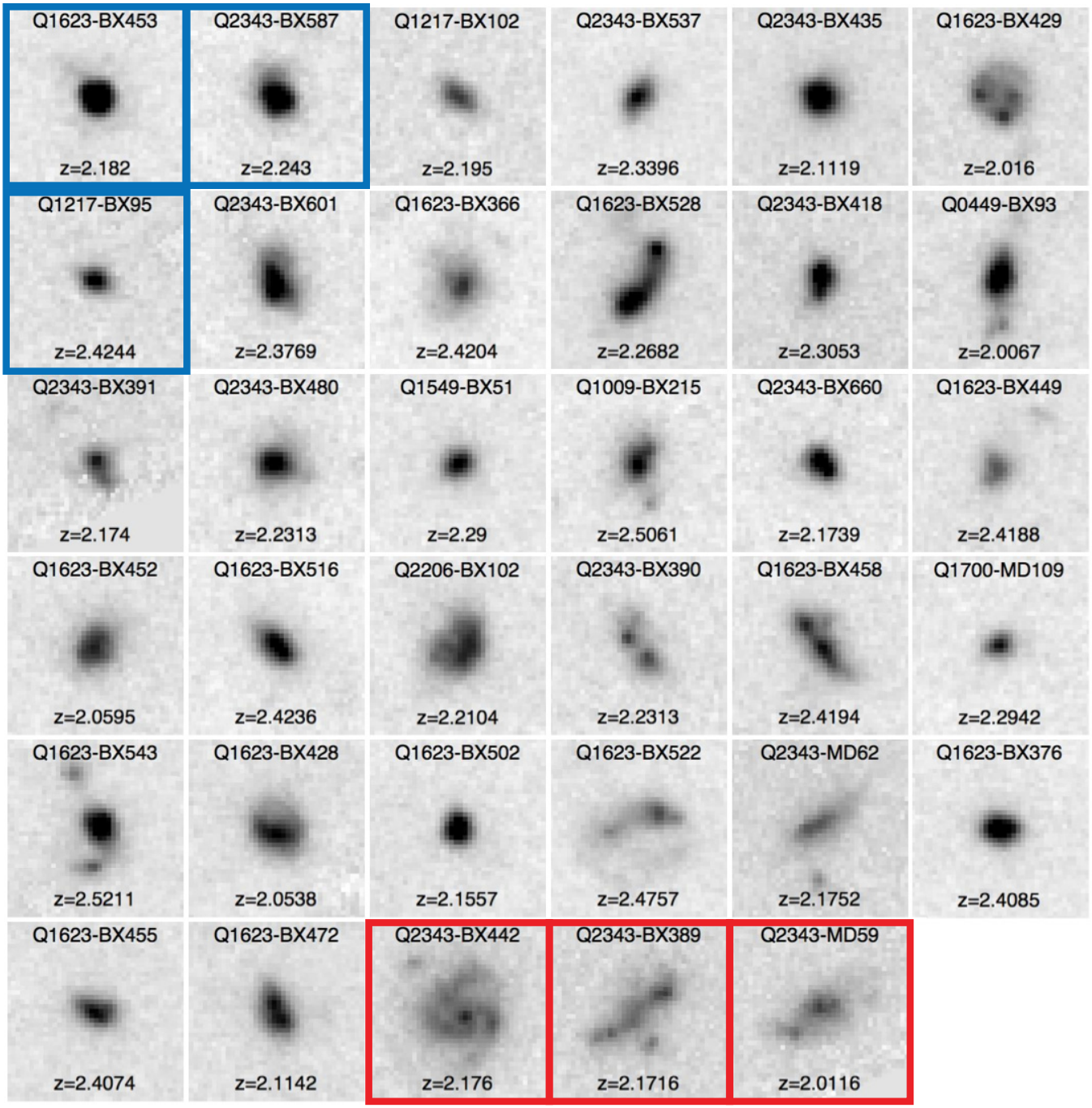

Figure 8. *HST*/WFC3 F160W morphologies of galaxies in the HAHQ sample (i.e., with Hα-derived systemic redshifts and high-quality UV spectra) sorted (left right, and top bottom) in order of declining velocity offset $\Delta v_{\rm IS}$. Blue boxes denote the three galaxies with the smallest semimajor axis radii in the HAHQ sample (Q1623-BX453, Q2343-BX587, Q1217-BX95), red boxes denote the three galaxies with the largest semimajor axis radii in the sample (Q2343-MD59, Q2343-BX442, Q2343-BX389). The largest three galaxies all have formal $\Delta v_{\rm IS} > 0$ km s^{-1}, while the smallest tend to be those with the most negative $-950 < \Delta v_{\rm IS} < -300$ km s^{-1}. As demonstrated in Figure 4, the small-r sample has a "younger" UV spectrum with significant Lyα emission. Individual postage stamps are 3″ to a side, oriented with north up and east left.

(A color version of this figure is available in the online journal.)

gas or stalled winds at large radii, although it most likely corresponds to cold gas located at small radii within the galaxy.

4.2. High-ionization Absorption Lines

In addition to the low-ionization absorption lines, the high-ionization transitions Si IV λ1393, Si IV λ1402, and C IV λ1550 are also systematically less blueshifted for larger galaxies. Combining measurements made from the two Si IV absorption lines,[18] we find that the mean blueshift of the high-ionization lines (HIS) is $\langle \Delta v_{\rm HIS} \rangle = -147 \pm 58$ km s^{-1} for the small-radius sample, but only $\langle \Delta v_{\rm HIS} \rangle = -21 \pm 40$ km s^{-1} for

[18] We neglect C IV in this stack since it is complicated by the superposition of interstellar absorption on a stellar-wind-induced P-Cygni profile.

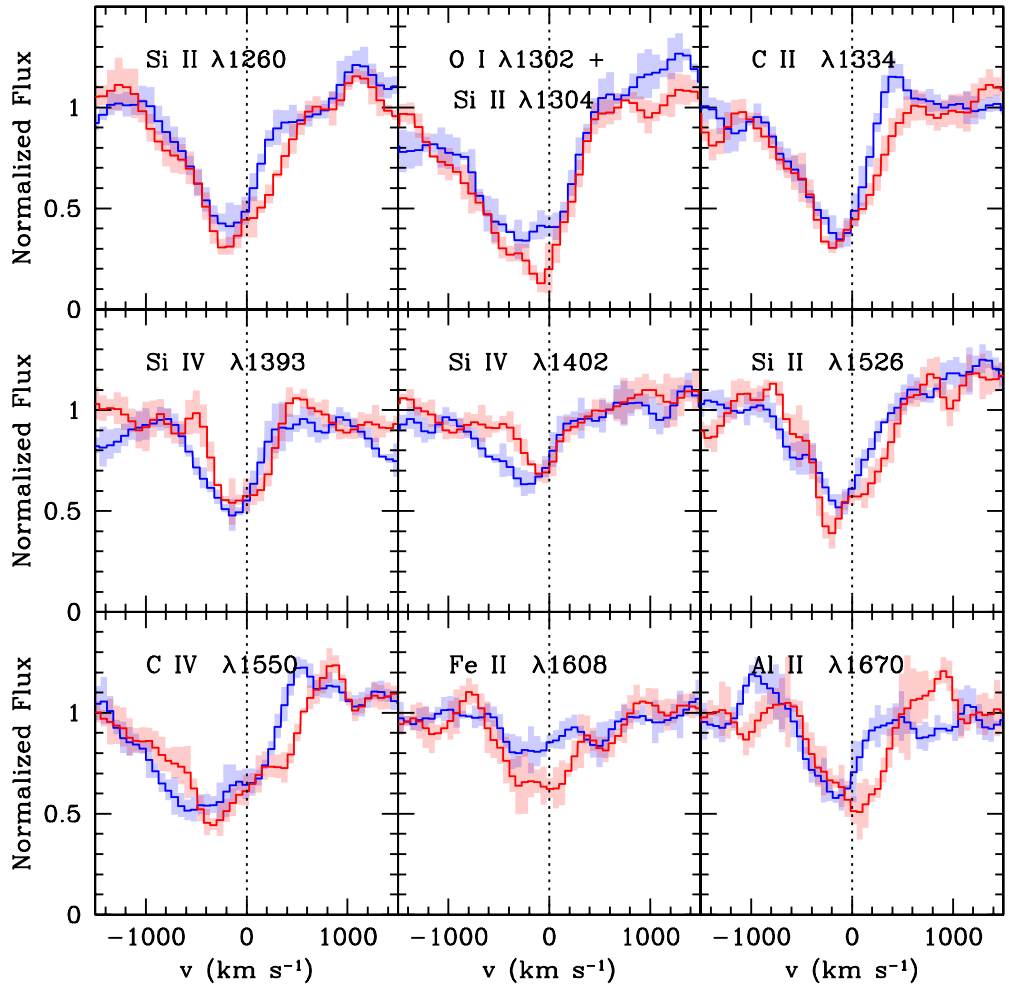

Figure 9. As Figure 4 (lower panel) but zoomed in to the central 1500 km s^{-1} surrounding each of the major low-ionization (Si II λ1260, O I λ1302 + Si II λ1304, C II λ1334, Si II λ1526, Fe II λ1608, Al II λ1670) and high-ionization (Si IV λ1393, Si IV λ1402, C IV λ1550) absorption line features. Blue/red lines respectively represent the stacked spectra of galaxies in the smallest/largest size bins for the HAHQ sample. Shaded regions indicate 1σ uncertainties estimated by Monte Carlo bootstrap resampling from the individual galaxies making up the composite spectra.

(A color version of this figure is available in the online journal.)

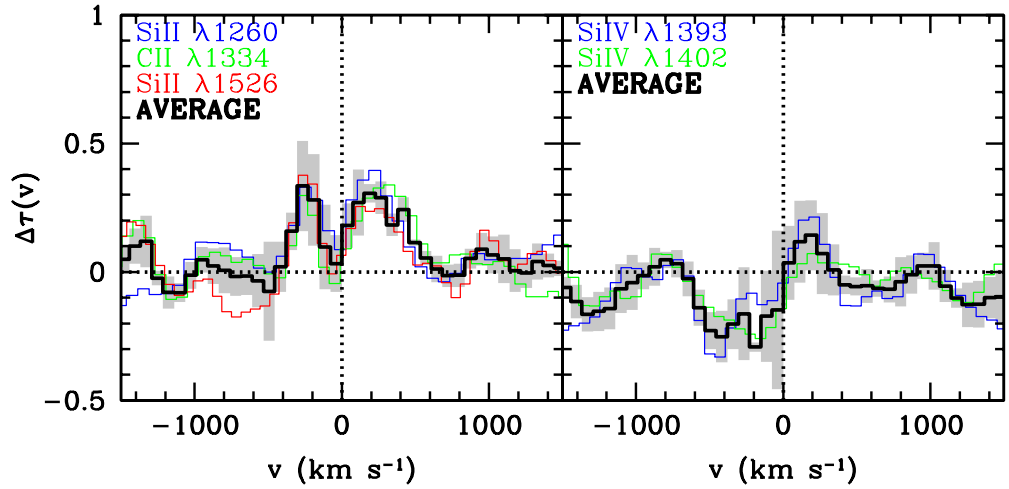

Figure 10. Additional optical depth $\Delta\tau(v)$ required to transform the low-r composite galaxy spectrum into the high-r composite as a function of offset from the systemic velocity. Left-hand panel: colored lines indicate the profiles derived for individual low-ionization interstellar (LIS) absorption lines, solid black line indicates the average of the three individual $\Delta\tau(v)$ profiles. Right-hand panel: colored lines indicate the profiles derived for Si IV λ1393 and λ1402 high-ionization interstellar (HIS) absorption lines, solid black line indicates the average of the two individual $\Delta\tau(v)$ profiles. Note that the LIS profiles show additional optical depth near $v \sim$ 0–200 km s^{-1} in large galaxies, while the HIS profiles show marginally *reduced* optical depth at relative velocities $-600 < v < 0$ km s^{-1}. Shaded gray regions indicate 1σ uncertainties estimated by Monte Carlo bootstrap resampling from the individual galaxies making up the composite spectra.

(A color version of this figure is available in the online journal.)

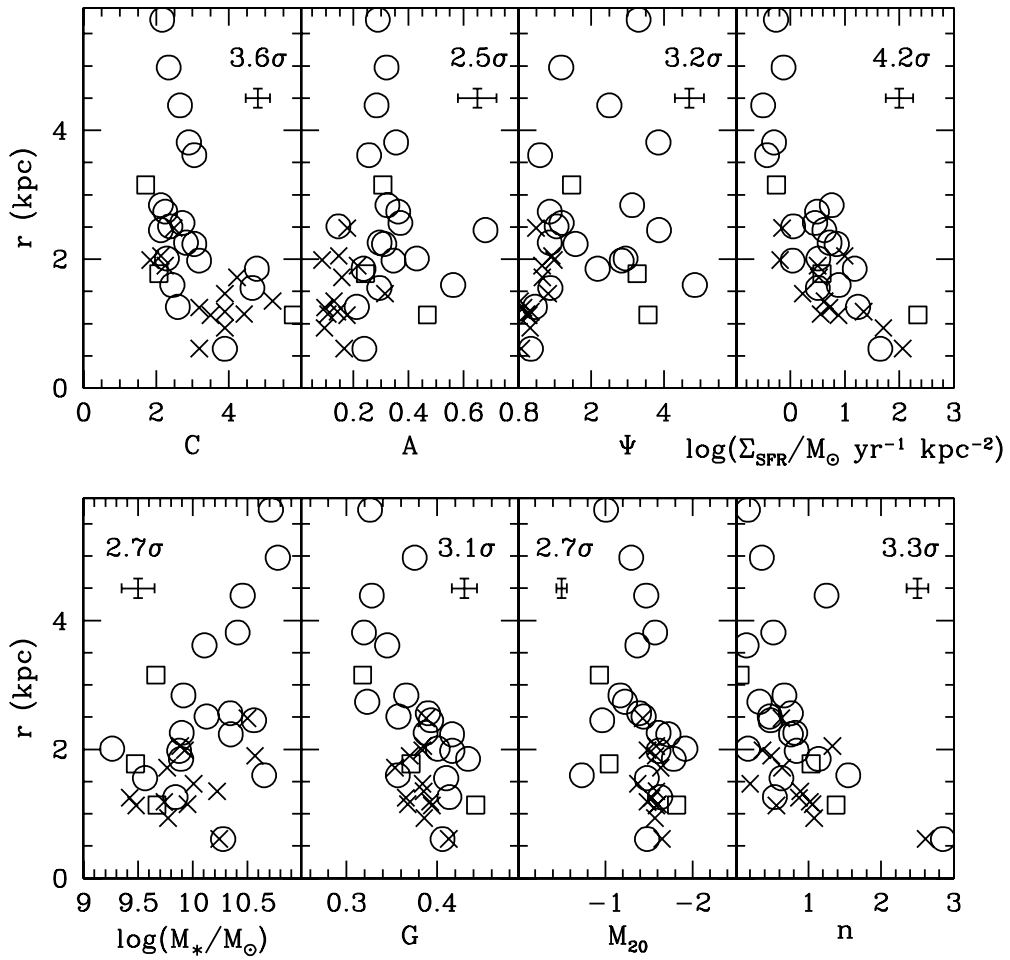

Figure 11. Correlations between semimajor axis radius r, stellar mass M_*, and the other morphological parameters. Symbols are as in Figure 7. Each panel quotes the statistical significance of the correlation on the basis of the Spearman rank correlation test. Error bars in each panel indicate the characteristic uncertainty of individual points.

the large-radius sample.[19] In contrast to the low-ionization lines however, this effect is not produced by an additional component of τ centered around $v \sim 0$ km s^{-1}, suggesting that the $v \sim 0$ km s^{-1} gas may be more strongly self-shielded than the majority of the outflowing gas. Instead, the large-radius subsample exhibits a weaker blue wing to the absorption profile (Figure 10), suggesting that highly ionized ($T \gtrsim 10^4$ K) gas may have lower peak outflow velocities in galaxies with rest-optical continuum radii $r \gtrsim 3$ kpc.

4.3. Fine Structure Emission

In addition to exhibiting stronger Lyα emission and more systematically blueshifted low-ionization absorption features, galaxies with smaller rest-optical continuum radii also have stronger fine structure emission lines. As indicated by Figure 4, Si II* λ1265 and λ1309 emission features are more prominent in composite spectra of galaxies with effective radii $r \lesssim 2$ kpc than in those with $r \gtrsim 3$ kpc (most noticeably in the composite stack from the parent sample, and to a lesser extent in the HAHQ composite stack). This result is consistent with the recent studies of Berry et al. (2012) and Jones et al. (2012), who respectively noted that Si II* increases with $W_{\mathrm{Ly}\alpha}$ and is stronger in star-forming galaxies at $z \sim 4$ than at lower redshifts (which Jones et al. 2012 ascribe to the increasing characteristic radius of low-ionization gas with cosmic time).

4.4. Correlation of Metal Lines with Other Morphological Statistics

As indicated in Figure 11, there are significant underlying correlations between r and the other morphological statistics. On average, galaxies with larger semimajor axis radii have larger M_*, shallower radial density profiles (lower n), less-concentrated light profiles (i.e., lower C and G), and tend to be more irregular (whether measured using M_{20}, A, or Ψ). Such generic trends are apparent in Figure 8; the largest galaxies tend to be those that show most morphological irregularity to the light profiles, while the smallest tend to be single well-nucleated sources.

The physical mechanism underlying the change in Δv_{IS} is the buildup of neutral gas at rest with respect to the stars (as discussed further in Section 5). The internal correlation of semimajor axis radius with other parameters, however, gives rise to a variety of correlations of marginal significance (see Table 3) between Δv_{IS} and stellar/baryonic mass, the six morphological statistics G, M_{20}, C, A, Ψ, r, and n, and the SFR surface density Σ_{SFR}. Given the known positive correlation between mass and effective radius for the galaxies in our sample (Nagy et al. 2011; Paper I), it is perhaps unsurprising that similar qualitative trends in UV spectral features are observed when

[19] Uncertainties represent 1σ uncertainties in the mean combining Δv_{HIS} of individual galaxy spectra.

the galaxy sample is subdivided according to either mass or radius. Likewise, although there is no significant correlation of $\Delta v_{\rm IS}$ with the total SED-derived SFR (in part since all galaxies in our sample are selected on the basis of rest-UV color to be actively star forming with SFR $\gtrsim 2\,M_{\odot}$ yr^{-1}), there is a correlation at the $>2\sigma$ level with the SFR surface density in the sense that galaxies with higher $\Sigma_{\rm SFR}$ tend to be missing the $v \sim 0$ km s^{-1} absorption component (see Figure 7, right-hand panel).[20] Similarly, there is a $\sim 2\sigma$ correlation of $\Delta v_{\rm IS}$ with stellar population age in the sense that older populations have the strongest $v \sim 0$ km s^{-1} absorption component, consistent with our finding that the $r < 1.95$ and $r > 1.95$ kpc samples have mean ages of 260 and 740 Myr, respectively.

5. DISCUSSION

Steidel et al. (2010) suggested that the physical property governing both Lyα emission properties and interstellar absorption line kinematics was baryonic mass, which correlated with $\Delta v_{\rm IS}$ with a significance of 2.7σ in their sample of 73 galaxies. Since galaxies with higher baryonic masses tend to have older stellar populations and greater total quantities of interstellar gas, this additional gas may naturally lead to greater covering fractions and longer scattering paths, suppressing Lyα emission and making interstellar absorption lines deeper.

In detail though, mass may not be the most predictive indicator of the spectroscopic properties of a given galaxy. Although the correlation that we find between $\Delta v_{\rm IS}$ and r is of comparable statistical significance (2.6σ) to the baryonic mass correlation described by Steidel et al. (2010), this may simply be because there are $\sim$ a factor of two fewer galaxies in the morphological HAHQ sample. Replicating the HAHQ sample to a total sample size of 73 galaxies with random resampling using a Monte Carlo algorithm (repeated 10,000 times), we estimate that the expected correlation significance between r and $\Delta v_{\rm IS}$ in a sample of the size of Steidel et al. (2010) is $3.8 \pm 0.7\,\sigma$. Indeed, while the galaxies with the strongest/weakest $\Delta v_{\rm IS}$ occupy an overlapping range of $M_{\rm bary}$ (the galaxy with the *weakest* $\Delta v_{\rm IS}$ in our HAHQ sample has a baryonic mass smaller than the galaxy with the *strongest* $\Delta v_{\rm IS}$), these galaxies have clearly distinct visual morphologies (Figure 8). Likewise, although the galaxies with the highest $\Sigma_{\rm SFR}$ are those with the strongest $\Delta v_{\rm IS}$ (consistent with theoretical expectations that galaxies with a higher concentration of supernovae should be capable of more completely expelling the local ISM), this correlation is driven entirely by the (stronger) relation between r and $\Delta v_{\rm IS}$ and the definition $\Sigma_{\rm SFR} = {\rm SFR}/r^2$ (although cf. Kornei et al. 2012 for star-forming galaxies at $z \sim 1$).

All of the correlations detailed herein may therefore simply be byproducts of a single underlying physical mechanism: the growth of an extended disk. Star-forming $z \sim$ 2–3 galaxies with low-to-moderate stellar mass (i.e., $M_* \lesssim 10^{10}\,M_{\odot}$) tend to be compact, young, triaxial systems whose kinematics are dominated by velocity dispersion rather than rotation about a preferred kinematic axis. High $\Sigma_{\rm SFR}$ within these systems drives strong gaseous outflows into the surrounding intergalactic medium (IGM) and suppresses the buildup of a stable ISM. In time, the increasing stellar mass formed by these galaxies is able to stabilize the formation of an extended (albeit still thick) gaseous disk (as proposed by, e.g., Martig & Bournaud 2010) in which the overall gas fraction decreases ($f_{\rm gas}$ is anti-correlated with $\Delta v_{\rm IS}$ with a confidence of 2.8σ in the HAHQ sample) and systemic rotation becomes an increasingly important means of dynamical support. The lower $\Sigma_{\rm SFR}$ in this extended disk is no longer able to expel gas as efficiently, a large component of which remains close to the galaxy and serves to both extinguish the Lyα emission (or resonantly scatter it to larger radii) and superimpose a zero-velocity absorption component atop the stellar continuum emission.

While the growth of such extended structure is naturally associated with both evolving M_* and $\Sigma_{\rm SFR}$, there is not a single well-defined value of either that demarcates the transition, and the mass at which extended structures may be supported can vary significantly based on the merger histories and other details of individual galaxies. In contrast, rest-frame optical size r characterizes where the transition to an extended disk has *already occurred*. From a phenomenological standpoint, rest-optical morphology may therefore be the most robust and accessible means of identifying systems for which feedback is less efficient at evacuating gas from the galaxy.

This physical picture necessarily suggests that the zero-velocity gas feature should become more pronounced (i.e., $\Delta v_{\rm IS}$ is less strongly blueshifted) as the contribution of rotational shear to the dynamical support of a galaxy increases. Such trends have already been noted in samples of galaxies observed with either long-slit (see Figure 2 of Steidel et al. 2010) or IFU spectroscopy (see Figure 13 of Law et al. 2009). More recently, Förster Schreiber et al. (2011a) presented *HST*/NICMOS morphologies of a sample of six galaxies observed previously with the SINFONI integral-field spectrograph. Of these six galaxies, five are representative of the most disk-like known systems at $z \sim 2$ based on their observed kinematics (the other galaxy is identified as a major merger). These five galaxies[21] all lie at the upper edge of the distribution of effective radii for $z \sim$ 2–3 star-forming galaxies (see colored circles in Figure 13 of Paper I) and have a mean $\langle \Delta v_{\rm IS} \rangle = -4$ km s^{-1} (excluding Q1623-BX663, whose rest-UV spectra are complicated by AGN features). These systems can therefore be identified from the overall $z \sim$ 2–3 galaxy sample by both their semimajor axis radii and spatially resolved velocity shear, but not by their stellar masses, which are widely distributed in the range $M_* = 8 \times 10^9$–$1 \times 10^{11}\,M_{\odot}$.

Steidel et al. (2010) suggested that the anti-correlation between $\Delta v_{\rm IS}$ and velocity shear may be due in part to projection effects. If objects with the largest velocity gradients tend to be edge-on rotating disks, outflows from these galaxies might be expected to be collimated perpendicular to the disk so that there is simply little projection of the outflowing gas onto our line of sight (see, e.g., Chen et al. 2010; Bordoloi et al. 2011), while face-on systems would exhibit minimal rotation and maximum $\Delta v_{\rm IS}$. Such a correlation between inclination and outflow velocity was recently found for a sample of star-forming galaxies at $z \sim 1$ by Kornei et al. (2012). However, in our $z \sim 2$ sample we observe no correlation of $\Delta v_{\rm IS}$ with inclination as parameterized through the apparent minor/major axis ratio b/a for the 35 galaxies in our HAHQ sample (0.3σ from the null hypothesis; see Table 3). In part, the lack of correlation may simple reflect the irregularity of $z \sim 2$ star-forming galaxies and the difficulty of determining inclination robustly for these intrinsically triaxial (Paper I) systems. However, no significant difference is observed in $\Delta v_{\rm IS}$ even for the two most disk-like

[20] Kornei et al. (2012) find that $\Sigma_{\rm SFR}$ is more strongly correlated than galaxy size with $\Delta v_{\rm IS}$ for a sample of star-forming galaxies at $z \sim 1$.

[21] Q1623-BX663, SSA22a-MD41, Q2343-BX389, Q2343-BX610, and Q2346-BX482. One of these galaxies, Q2343-BX389, is also in our WFC3 sample.

galaxies in the sample. Morphology and IFU-derived kinematics suggest that Q2343-BX389 is consistent with an edge-on disk (Förster Schreiber et al. 2009), while Q2343-BX442 has both morphology and IFU kinematics consistent with a nearly face-on ($i = 42^\circ \pm 10^\circ$) disk with spiral substructure (see discussion by Law et al. 2012b). Despite their different orientations both galaxies have $\Delta v_{\rm IS} \sim 0$ km s^{-1}, suggesting either that $\Delta v_{\rm IS}$ is uncorrelated with inclination or that the opening angle of the outflow is less than $\sim 40^\circ$.

As illustrated by Figure 10 much of the additional absorption in the largest galaxies has positive velocity $\sim$0–400 km s^{-1} with respect to the systemic redshift, and formally $\Delta v_{\rm IS} > 0$ km s^{-1} for the three galaxies with largest semimajor axis radii in our HAHQ sample (Q2343-MD59, Q2343-BX442, Q2343-BX389). It is therefore possible that absorption line spectroscopy of the largest galaxies is tracing *infalling* gas, whether from a recent merger, recycled wind accretion (e.g., Oppenheimer et al. 2010) or from cold cosmological flows (e.g., Dekel et al. 2009; Kereš et al. 2009). While such inflows are one plausible mechanism for solving the gas fueling problem, it is unclear why such accretion (presumably with a small covering fraction) would cause the near-complete absorption of Lyα (see discussion by Steidel et al. 2010). Similarly, simulations (e.g., Dekel & Birnboim 2006; Kereš et al. 2009) generally predict that such cold flows should be suppressed in the most massive galaxies at $z > 2$, in contrast to our observation that $\Delta v_{\rm IS} > 0$ km s^{-1} occurs more commonly for large and massive galaxies.

6. SUMMARY

We have demonstrated that rest-optical morphology is correlated with the gas-phase properties of $z \sim 2$ star-forming galaxies as traced by their rest-UV spectra. Lyα emission is most commonly observed in galaxies with small rest-optical half-light radii ($r < 2$ kpc), and the equivalent width $W_{\rm Ly\alpha}$ of the emission is correlated with half-light radius with $>2\sigma$ confidence. Although some large-r galaxies with Type III morphology (i.e., extended and diffuse) show Lyα in emission, this emission is relatively weak; the 12 galaxies in our sample with $W_{\rm Ly\alpha} > 30$ Å all have small half-light radii ($r < 2$ kpc) and Type I or Type II morphologies (i.e., compact clumps). This correlation is independent of the better-known relations between $W_{\rm Ly\alpha}$, dust content, and SFR. Additionally, all galaxies in our spectroscopic sample for which Lyα is observed in emission and no absorption lines are present in the rest-UV spectrum have morphological Type II (i.e., consist of two or more clumps of emission separated from each other by $\sim$1 arcsec), suggesting that slit losses of continuum light from these galaxies may be significant.

Combining our results with those previously published in the literature (e.g., Steidel et al. 2010, Pentericci et al. 2010, Kornei et al. 2010), the broad picture of $z \sim 2$–3 star-forming galaxies is relatively clear. Galaxies with Lyα emission tend to be physically smaller than galaxies with negligible Lyα emission, with lower stellar mass, less dust, lower SFRs, and a slightly greater degree of nucleation in the rest-frame UV and optical light distribution.

Using a subsample of 35 galaxies with both high-quality rest-UV spectra and Hα-derived systemic redshifts we have found that galaxy morphology is also correlated with the median blueshift of interstellar absorption line features $\Delta v_{\rm IS}$ with 2.6σ significance. Although similar blue wings in the low-ionization absorption line profiles indicate that galaxies of all morphological types drive comparably strong outflows at speeds up to $\sim$800 km s^{-1} into their surrounding environments, increasing optical half-light radius is accompanied by an increase in optical depth around the systemic redshift of the galaxy. This finding is similar in statistical significance to trends with increasing baryonic mass described recently by Steidel et al. (2010), but may be of physically greater importance considering the smaller sample size. While galaxies with $\Delta v_{\rm IS}$ differing by almost 1000 km s^{-1} can have baryonic masses identical to within observational uncertainty, such galaxies have clearly distinct morphologies spanning the range from compact clumps to extended disks.

The increased optical depth arises in gas nearly at rest with respect to the systemic redshift, in close physical proximity to the galaxy, and apparently corresponding to an extended disk of optical continuum light. This stronger $v \sim 0$ km s^{-1} component is responsible both for the shifting absorption line profile and the attenuation of $W_{\rm Ly\alpha}$ (via a longer resonant scattering path) in galaxies with larger rest-optical half-light radii. The $v \sim 0$ km s^{-1} absorption component is not present in the higher-ionization features Si IV λ1393 and 1402, however, suggesting that this gas may be more strongly self-shielded than the majority of the outflowing gas.

In contrast to recent results at lower redshifts (e.g., Kornei et al. 2012), there is no obvious relation between $\Delta v_{\rm IS}$ and galaxy inclination as parameterized by the axis ratio b/a for the 35 galaxies in our HAHQ sample. In part this may be due to the difficulty determining robust inclinations for inherently triaxial star-forming systems. Even for two particularly well-resolved galaxies with visual morphology and IFU kinematics consistent with face-on and edge-on disks, however, there are no obvious differences in the outflowing gas kinematics (although the quality of individual spectra prohibits a detailed analysis of just these two galaxies). There is therefore no evidence to support a classical bipolar outflow model for star-forming galaxies at $z \sim 2$–3. This may be because such galaxies are in the process of transforming from clumpy, irregular systems to more regular (albeit thick) disks, and outflowing gas at high velocities and large distances from the galaxy may predate establishment of the disk and its corresponding polar axis.

In general, our observations are consistent with inside-out growth of star-forming galaxies in the young universe: "typical" $z \sim 2$ star-forming galaxies appear to be gas-rich, compact, triaxial systems that are dominated by velocity dispersion between individual star-forming regions rather than systemic rotation, and whose high $\Sigma_{\rm SFR}$ drives strong outflows into the surrounding IGM. As these galaxies mature they gain stellar mass, stabilizing the formation of extended (albeit still thick) gaseous disks in which rotational support is observed to play an increasing role. As the star formation migrates from central regions into these extended disks the $\Sigma_{\rm SFR}$ drops and is no longer capable of expelling gas from the galaxy as efficiently.

We caution, however, that it is challenging to generalize about the relation between rest-optical morphology and gas-phase kinematics for the entire $z \sim 2$ star-forming sample on the basis of the relatively small number of galaxies in our sample. A major limiting factor is systemic nebular redshifts, without which we cannot quantify the outflow velocities. Although $\sim$100 $z \sim 2$–3 star-forming galaxies with rest-UV spectra in the KBSS have had systemic redshifts derived from nebular emission line spectroscopy (e.g., Erb et al. 2006b; Law et al. 2009), only a fraction of these galaxies fell within the footprint of our *HST*/WFC3 imaging survey. In the future it will be possible to explore these trends in much greater detail with the aid of multi-object

near-IR and optical spectrographs; using these it will be possible to obtain Hα redshifts and outflow kinematics efficiently for large and diverse samples of galaxies in fields that have already been imaged with *HST*.

D.R.L., C.C.S., and S.R.N. have been supported by grant GO-11694 from the Space Telescope Science Institute, which is operated by the Association of Universities for Research in Astronomy, Inc., for NASA, under contract NAS 5-26555. C.C.S. has been supported by the US National Science Foundation through grants AST-0606912 and AST-0908805. A.E.S. acknowledges support from the David and Lucile Packard Foundation. Finally, we extend thanks to those of Hawaiian ancestry on whose sacred mountain we are privileged to be guests.

REFERENCES

Abraham, R. G., van den Bergh, S., & Nair, P. 2003, ApJ, 588, 218
Adelberger, K. L., Steidel, C. C., Shapley, A. E., et al. 2004, ApJ, 607, 226
Berry, M., Gawiser, E., Guaita, L., et al. 2012, ApJ, 749, 4
Bershady, M. A., Jangren, A., & Conselice, C. J. 2000, AJ, 119, 2645
Bond, N. A., Gawiser, E., Gronwall, C., et al. 2009, ApJ, 705, 639
Bordoloi, R., Lilly, S. J., Knobel, C., et al. 2011, ApJ, 743, 10
Bournaud, F., & Elmegreen, B. G. 2009, ApJ, 694, L158
Bournaud, F., Elmegreen, B. G., & Elmegreen, D. M. 2007, ApJ, 670, 237
Calzetti, D., Armus, L., Bohlin, R. C., et al. 2000, ApJ, 533, 682
Ceverino, D., Dekel, A., & Bournaud, F. 2010, MNRAS, 404, 2151
Chabrier, G. 2003, PASP, 115, 763
Chen, Y.-M., Tremonti, C. A., Heckman, T. M., et al. 2010, AJ, 140, 445
Conselice, C. J. 2003, ApJS, 147, 1
Conselice, C. J., Bershady, M. A., & Jangren, A. 2000, ApJ, 529, 886
Conselice, C. J., Blackburne, J. A., & Papovich, C. 2005, ApJ, 620, 564
Dekel, A., & Birnboim, Y. 2006, MNRAS, 368, 2
Dekel, A., Birnboim, Y., Engel, G., et al. 2009, Nature, 457, 451
Dickinson, M., Papovich, C., Ferguson, H. C., & Budavári, T. 2003, ApJ, 587, 25
Elmegreen, B. G., Bournaud, F., & Elmegreen, D. M. 2008, ApJ, 688, 67
Elmegreen, B. G., & Elmegreen, D. M. 2006, ApJ, 650, 644
Elmegreen, D. M., Elmegreen, B. G., Rubin, D. S., & Schaffer, M. A. 2005, ApJ, 631, 85
Erb, D. K. 2008, ApJ, 674, 151
Erb, D. K., Shapley, A. E., Pettini, M., et al. 2006a, ApJ, 644, 813
Erb, D. K., Steidel, C. C., Shapley, A. E., et al. 2006b, ApJ, 647, 128
Erb, D. K., Steidel, C. C., Shapley, A. E., et al. 2006c, ApJ, 646, 107
Förster Schreiber, N. M., Genzel, R., Bouché, N., et al. 2009, ApJ, 706, 1364
Förster Schreiber, N. M., Shapley, A. E., Erb, D. K., et al. 2011a, ApJ, 731, 65
Förster Schreiber, N. M., Shapley, A. E., Genzel, R., et al. 2011b, ApJ, 739, 45
Gawiser, E., Francke, H., Lai, K., et al. 2007, ApJ, 671, 278
Genzel, R., Burkert, A., Bouché, N., et al. 2008, ApJ, 687, 59
Genzel, R., Newman, S., Jones, T., et al. 2011, ApJ, 733, 101
Genzel, R., Tacconi, L. J., Eisenhauer, F., et al. 2006, Nature, 442, 786
Immeli, A., Samland, M., Gerhard, O., & Westera, P. 2004a, A&A, 413, 547
Immeli, A., Samland, M., Westera, P., & Gerhard, O. 2004b, ApJ, 611, 20
Jones, T., Stark, D. P., & Ellis, R. S. 2012, ApJ, 751, 51
Kennicutt, R. C., Jr. 1998a, ARA&A, 36, 189
Kennicutt, R. C., Jr. 1998b, ApJ, 498, 541
Kereš, D., Katz, N., Fardal, M., Davé, R., & Weinberg, D. H. 2009, MNRAS, 395, 160
Kereš, D., Katz, N., Weinberg, D. H., & Davé, R. 2005, MNRAS, 363, 2
Komatsu, E., Smith, K. M., Dunkley, J., et al. 2011, ApJS, 192, 18
Kornei, K. A., Shapley, A. E., Erb, D. K., et al. 2010, ApJ, 711, 693
Kornei, K. A., Shapley, A. E., Martin, C. L., et al. 2012, ApJ, submitted (arXiv:1205.0812)
Kulas, K. R., Shapley, A. E., Kollmeier, J. A., et al. 2012, ApJ, 745, 33
Law, D. R., Shapley, A. E., Steidel, C. C., et al. 2012a, Nature, 487, 338
Law, D. R., Steidel, C. C., Erb, D. K., et al. 2007a, ApJ, 656, 1
Law, D. R., Steidel, C. C., Erb, D. K., et al. 2007b, ApJ, 669, 929
Law, D. R., Steidel, C. C., Erb, D. K., et al. 2009, ApJ, 697, 2057
Law, D. R., Steidel, C. C., Shapley, A. E., et al. 2012b, ApJ, 745, 85
Lotz, J. M., Davis, M., Faber, S. M., et al. 2008a, ApJ, 672, 177
Lotz, J. M., Jonsson, P., Cox, T. J., & Primack, J. R. 2008b, MNRAS, 391, 1137
Lotz, J. M., Madau, P., Giavalisco, M., Primack, J., & Ferguson, H. C. 2006, ApJ, 636, 592
Lotz, J. M., Primack, J., & Madau, P. 2004, AJ, 128, 163
Malhotra, S., Rhoads, J. E., Finkelstein, S. L., et al. 2012, ApJ, 750, L36
Martig, M., & Bournaud, F. 2010, ApJ, 714, L275
Nagy, S. R., Law, D. R., Shapley, A. E., & Steidel, C. C. 2011, ApJ, 735, L19
Noguchi, M. 1999, ApJ, 514, 77
Oppenheimer, B. D., Davé, R., Kereš, D., et al. 2010, MNRAS, 406, 2325
Peng, C. Y., Ho, L. C., Impey, C. D., & Rix, H.-W. 2002, AJ, 124, 266
Peng, C. Y., Ho, L. C., Impey, C. D., & Rix, H.-W. 2010, AJ, 139, 2097
Pentericci, L., Grazian, A., Scarlata, C., et al. 2010, A&A, 514, A64
Pettini, M., Steidel, C. C., Adelberger, K. L., Dickinson, M., & Giavalisco, M. 2000, ApJ, 528, 96
Rauch, M., Becker, G. D., Haehnelt, M. G., et al. 2011, MNRAS, 418, 1115
Ravindranath, S., Giavalisco, M., Ferguson, H. C., et al. 2006, ApJ, 652, 963
Reddy, N. A., Erb, D. K., Pettini, M., Steidel, C. C., & Shapley, A. E. 2010, ApJ, 712, 1070
Reddy, N. A., Pettini, M., Steidel, C. C., et al. 2012, ApJ, 754, 25
Reddy, N. A., Steidel, C. C., Erb, D. K., Shapley, A. E., & Pettini, M. 2006, ApJ, 653, 1004
Reddy, N. A., Steidel, C. C., Pettini, M., et al. 2008, ApJS, 175, 48
Rees, M. J., & Ostriker, J. P. 1977, MNRAS, 179, 541
Robertson, B., Bullock, J. S., Cox, T. J., et al. 2006, ApJ, 645, 986
Schade, D., Lilly, S. J., Crampton, D., et al. 1995, ApJ, 451, L1
Sérsic, J. L. 1963, Bol. Asociacion Argentina Astron. La Plata Argentina, 6, 41
Shapley, A. E., Steidel, C. C., Adelberger, K. L., et al. 2001, ApJ, 562, 95
Shapley, A. E., Steidel, C. C., Erb, D. K., et al. 2005, ApJ, 626, 698
Shapley, A. E., Steidel, C. C., Pettini, M., & Adelberger, K. L. 2003, ApJ, 588, 65
Steidel, C. C., Adelberger, K. L., Shapley, A. E., et al. 2003, ApJ, 592, 728
Steidel, C. C., Bogosavljević, M., Shapley, A. E., et al. 2011, ApJ, 736, 160
Steidel, C. C., Erb, D. K., Shapley, A. E., et al. 2010, ApJ, 717, 289
Steidel, C. C., Shapley, A. E., Pettini, M., et al. 2004, ApJ, 604, 534
Swinbank, A. M., Papadopoulos, P. P., Cox, P., et al. 2011, ApJ, 742, 11
Tacconi, L. J., Genzel, R., Neri, R., et al. 2010, Nature, 463, 781
Trainor, R. F., & Steidel, C. C. 2012, ApJ, 752, 39
van de Voort, F., & Schaye, J. 2012, MNRAS, 423, 2991
Weiner, B. J., Coil, A. L., Prochaska, J. X., et al. 2009, ApJ, 692, 187
White, S. D. M., & Frenk, C. S. 1991, ApJ, 379, 52
White, S. D. M., & Rees, M. J. 1978, MNRAS, 183, 341
Wright, S. A., Larkin, J. E., Law, D. R., et al. 2009, ApJ, 699, 421
Wuyts, S., Förster Schreiber, N. M., Genzel, R., et al. 2012, ApJ, 753, 114
Wuyts, S., Förster Schreiber, N. M., van der Wel, A., et al. 2011, ApJ, 742, 96
Zhu, G., Moustakas, J., & Blanton, M. R. 2009, ApJ, 701, 86